Effects of oblique impacts on the impact strength of porous gypsum and glass spheres: Implications for the collisional disruption of planetesimals in thermal evolution

Yasui, Minami
Arakawa, Masahiko
Yoshida, Yusaku
Matsue, Kazuma
Takano, Shota

(Citation)
Icarus,335:113414

(Issue Date)
2020-01-01

(Resource Type)
journal article

(Version)
Accepted Manuscript

(URL)
https://hdl.handle.net/20.500.14094/90006963

Effects of Oblique Impacts on the Impact Strength of Porous Gypsum and Glass Spheres: Implications for the Collisional Disruption of Planetesimals in Thermal Evolution

Minami Yasui, Masahiko Arakawa, Yusaku Yoshida, Kazuma Matsue, Shota Takano

Graduate School of Science, Kobe University

1-1, Rokkodai-cho, Nada-ku, Kobe, Hyogo 657-8501, Japan

Tel: +81-78-803-5741

Fax: +81-78-803-5741

E-mail: minami.yasui@pearl.kobe-u.ac.jp

Manuscript pages: 63

Number of figures: 16

Number of tables: 4

17 **Proposed running head:** Oblique impacts of planetesimals in thermal evolution

18

19 **Corresponding author:**

20 Minami Yasui

21 Now at

22 Graduate School of Science, Kobe University

23 1-1, Rokkodai-cho, Nada-ku, Kobe, Hyogo 657-8501, Japan

24 Tel: +81-78-803-5741

25 Fax: +81-78-803-5741

26 E-mail: minami.yasui@pearl.kobe-u.ac.jp

Abstract

We conducted oblique impact experiments for porous gypsum spheres and glass spheres simulating primitive and consolidated rocky planetesimals, respectively, and we determined the effects of the impact angle on the impact strength of these rocky planetesimals. The targets were a porous gypsum sphere with a porosity of 50% and a glass sphere without porosity. A spherical polycarbonate projectile impacted the target at 2–7 km s^{-1} at an impact angle, θ, ranging from 90° (head-on collision) to 10° (grazing collision) by using a two-stage light-gas gun at Kobe University, Japan. The impact strength obtained at a head-on collision was 1330 J kg^{-1} for the porous gypsum target and 1090 J kg^{-1} for the glass target, and these values increased markedly with the decrease of the impact angle when the impact angle was smaller than a critical angle, θ_c; the obtained θ_c values were 30° for the porous gypsum target and 55° for the glass target. The normalized largest fragment mass (m_l/M_t) showed a good correlation with an effective specific energy ($Q_{eff} = Q \sin^2 \theta$); the subsequent empirical equation was $m_l/M_t = 10^{2.02} {Q_{eff}}^{0.76}$ for the porous gypsum target and $m_l/M_t = 10^{4.66} {Q_{eff}}^{1.68}$ at m_l/M_t <0.75 and $m_l/M_t = 10^{0.12} {Q_{eff}}^{0.08}$ at m_l/M_t >0.75 for the glass target. Based on our

experimental results, we successfully introduce the effects of an oblique impact on the degree of disruption for primitive and consolidated rocky planetesimals. Our findings demonstrate that in a strength-dominated regime, the catastrophic disruption can occur over a wide range of impact angles (30°–90°) irrespective of the target materials, when the specific energy at the collision is about four times larger than the impact strength.

Keywords: Collisional physics; Impact processes; Planetesimals; Planetary formation

1. Introduction

Solar system bodies are believed to grow via collisional disruption and re-accumulation processes among planetesimals that are in their early evolution. Planetesimals are speculated to have various porosities depending on their thermal evolution stages [e.g., *Neumann et al*., 2012; *Henke et al*., 2012; *Lichtenberg et al.*, 2016]. For example, planetesimals are believed to be parent bodies of porous asteroids and cometary nuclei, and they could therefore also be highly porous bodies [e.g., *Weidenschilling*, 1994, 2011; *Asphaug et al.*, 2002; *Sierks et al.*, 2011]. However, some planetesimals could experience various thermal processes such as shock metamorphism and aqueous alteration during their evolution so that they evolved to be low-porous or non-porous bodies. For the study of the collisional accretion processes of planetesimals in the solar nebula, the catastrophic disruption and the re-accumulation processes should be clarified for planetesimals that have various porosities depending on their thermal evolution.

There have been many experimental studies on the collisional processes of planetary bodies in attempts to determine the impact strength and the impact conditions for

66 catastrophic disruption and to measure the ejection velocity distribution of the impact
67 fragments, which is necessary for estimating the re-accumulation conditions. The prior
68 studies manipulated both projectile and target materials, and used basalt, glass, porous
69 gypsum, ice, and snow to examine the effects of porosity, inclusion, and static strength
70 on the impact strength. The size ratio of the projectile to the target, the target shape, the
71 target rotation rate, and the impact velocity were also manipulated to elucidate how these
72 parameters affect the impact strength and the ejection velocity of impact fragments [e.g.,
73 *Gault and Wedekind*, 1969; *Fujiwara et al.*, 1977; *Kawakami et al.*, 1983; *Arakawa*,
74 1999a; *Arakawa et al.*, 2002; *Okamoto and Arakawa*, 2009; *Yasui and Arakawa*, 2011;
75 *Morris and Burchell*, 2017]. Impact strength is defined as a specific energy when the
76 largest fragment mass is one-half of the original target mass, and the specific energy is
77 defined as the kinetic energy of the impactor per unit mass of the target.

78 It has been suspected that during the collisional evolution of planetesimals, they
79 collided obliquely with each other; this expectation arose because *Shoemaker* [1962]
80 calculated the probability of oblique impacts, P, among planetary bodies in the solar
81 system as $dP = 2\sin\theta\cos\theta d\theta$, where θ is the impact angle. Shoemaker demonstrated

82 that when the normal impact was defined as 90°, impact angle showing the maximum
83 frequency was 45° and the probability of collisions at an impact angle <70° was
84 approximately 90%. Many numerical simulations have thus been conducted for
85 planetesimal collisions at various impact angles [e.g., *Leinhardt and Richardson*, 2002;
86 *Movshovitz et al.*, 2016; *Genda et al.*, 2017], but only a few experimental studies have
87 been conducted to investigate the effect of the impact angle [e.g., *Fujiwara and*
88 *Tsukamoto*, 1980; *Nakamura,* 1993; *Arakawa,* 1999a]. Most of the experimental studies
89 examined head-on collisions; only a few experimental studies have investigated the effect
90 of the impact angle. It is necessary to study oblique impacts in the laboratory in order to
91 confirm and improve these numerical studies.

92 A few experimental studies have investigated the effect of the impact angle on the
93 impact strength and the ejection velocity of impact fragments. *Fujiwara and Tsukamoto*
94 [1980] conducted impact experiments using spherical basalt targets at the impact velocity
95 of 2.5–2.9 km s^{-1} and at impact angles from 0° to 60° (their impact angle of 0° indicates
96 a head-on collision). They obtained the relationship between the mass fraction of the
97 largest fragment to the original target and the specific energy, and they observed that the

98 mass fraction increased with the increase of the impact angle at a constant specific energy.
99 They also obtained the relationship between the fragment velocity at the antipodal point
100 of the impact point on the target and the specific energy, and they observed that the
101 antipodal velocity for an oblique impact was lower than that for a head-on collision.
102 *Nakamura* [1993] also conducted impact experiments using spherical basalt targets at the
103 impact velocity of 3.1–3.6 km s^{-1} and at impact angles from 30° to 90° (her impact angle
104 of 90° indicates a head-on collision). She obtained three-dimensional fragment velocities
105 and the cumulative mass distribution of impact fragments. However, both *Fujiwara and*
106 *Tsukamoto* [1980] and *Nakamura* [1993] carried out only five or six shots for oblique
107 impacts, because they conducted mainly head-on impact experiments. It is thus difficult
108 to discuss the effects of the impact angle on the impact strength and the ejection velocity
109 of impact fragments quantitatively.
110 *Arakawa* [1999a] conducted impact experiments in a cold room at –18°C by using
111 spherical H_2O ice targets at the impact velocity of 0.17–0.64 km s^{-1} and at impact angles
112 from 0° to 50° (his impact angle of 0° indicates a head-on collision). He studied the
113 ejection velocity distribution of impact fragments ejected from different positions on the

114 target surface, and he observed that the position showing the minimum ejection velocity
115 gradually shifted from the antipodal point to the upstream direction as the impact angle
116 was increased. He also noted that the minimum ejection velocity decreased with the
117 increase of the impact angle. He obtained an empirical equation for the minimum ejection
118 velocity, $V_{\min}$, related to the impact angle, ϕ, as $V_{\min} = 49(\cos\phi)^{3.4}$, but he did not
119 study the effect of oblique impacts on the impact strength of the ice target. Systematic
120 impact experiments investigating catastrophic disruption by oblique impacts are thus
121 necessary to determine not only the impact strength but also the ejection velocity of
122 impact fragments.

123 In this study, we conducted oblique impact experiments to study the effects of the
124 impact angle on the impact strength and the ejection velocity of impact fragments. We
125 systematically changed the impact angle from a head-on collision to a grazing collision.
126 We greatly increased the number of experiments for oblique impacts compared to three
127 previous works [*Fujiwara and Tsukamoto*, 1980; *Nakamura*, 1993; *Arakawa*, 1999a] in
128 order to determine the catastrophic disruption of oblique impacts quantitatively. We used
129 a porous gypsum target and a glass target for the experiments to simulate the collision of

130 rocky planetesimals in thermal evolution: the porous gypsum target simulated primitive
131 rocky planetesimals with high porosity before thermal evolution, and the glass target
132 simulated consolidated rocky planetesimals after thermal evolution. Based on our
133 experimental results and the theory of oblique impacts on planetary bodies described by
134 *Shoemaker* [1962], we also discuss the relationship between the impact probability and
135 the degree of impact disruption for rocky planetesimals depending on the thermal
136 evolution in the solar system.
137
138 **2. Experimental Methods**
139 *2.1. The targets and projectile*
140 We used a porous gypsum sphere and a glass sphere as targets simulating primitive
141 and consolidated rocky planetesimals, respectively. These materials have been used in
142 other laboratory experiments as the analogs of primitive and consolidated planetesimals
143 that have experienced thermal evolution at various stages [e.g., *Gault and Wedekind*,
144 1969; *Love et al.*, 1993; *Onose and Fujiwara*, 2004; *Fujii and Nakamura*, 2009; *Kadono*
145 *et al.*, 2009; *Nakamura et al.*, 2009; *Okamoto and Arakawa*, 2009; *Heißelmann et al.*,

146 2010; *Yasui and Arakawa*, 2011; *Yasui et al.*, 2012].

147 The porous gypsum sphere was prepared as follows. Commercial $CaSO_4 \cdot 1/2H_2O$
148 powder (Nitto Co., Ltd.) was mixed with tap water, and the mixed slurry was then put
149 into a spherical mold. The target was hung by a string in a recovery box, and a small clip
150 for hanging the string was set on the surface of the mixed slurry in the mold. After the
151 slurry was consolidated, the porous gypsum sphere was pulled out from the mold. It was
152 dried in an oven at 55°C for 2–7 days to complete the chemical reaction to $CaSO_4 \cdot 2H_2O$
153 and to remove excess water inside the sphere. The porosity of the porous gypsum spheres
154 was thus regulated at 55±6%; the bulk density was 983±131 kg m^{-3}. The tensile strength
155 and the bulk sound velocity of the porous gypsum changed from 2.56 MPa and 1.46 ×
156 10^3 m s^{-1} at the porosity of 49% to 1.01 MPa and 1.19 × 10^3 m s^{-1} at the porosity of 61%.
157 Although the impact strength and the ejection velocity of impact fragments could be
158 controlled by the porosity, i.e., the tensile strength, we found that a porosity variation of
159 10% or less did not affect the impact strength and the ejection velocity very much. The
160 diameter of the porous gypsum spheres was changed from 40 to 70 mm in 10 mm steps,
161 and the spheres with diameters of 40 and 60 mm were used only for the head-on collision

because the specific energy was changed in the wide range to determine the impact strength accurately.

The glass spheres were commercially available synthetic quartz glass spheres with diameters of 30, 50, 60, and 80 mm (Nichika Inc.), and the 60 mm-diameter sphere was used only for the head-on collision. The bulk density of the glass spheres was measured as 2513±33 kg m^{-3}. The bulk sound velocity of each glass sphere was 4.20×10^3 m s^{-1}. The reported tensile strength of soda lime glass, 31–35 MPa, was taken as the tensile strength for the glass sphere, since the bulk densities of the glass spheres were very similar to those of soda lime glass [*Ashby*, 2013]. A lattice pattern was painted on the target surface with black ink to identify the original position of each impact fragment recovered after the shot. The projectile was a polycarbonate sphere with a diameter of 4.73 (±0.01) mm and a mass, m_p, of 67.9 (±0.1) mg.

2.2. Impact experiments

We conducted impact experiments by using a two-stage light-gas gun set at Kobe University. Fig. 1 is a schematic illustration of the experimental setup. The vacuum

Fig. 1

chamber was evacuated at approximately 20 Pa before the shot. The impact angle, θ, was changed from 9° to 90°. The θ is defined as the angle between the line perpendicular to the projectile trajectory and the line linking the center of the target and the impact point on the target surface, as shown in Fig. 2a. We measured the impact angle by using images taken by a shutter camera or a high-speed camera. The offset of the projectile trajectory in the sight of the view is within the projectile's radius so we could ignore the offset to determine the impact angle. An overview of the method used to measure the impact angle θ is shown in Figs. 2b and 2c. When the shutter camera was used with an exposure time of 100 ns (Fig. 2b), two images were taken at different times before the impact, and the impact point on the target surface was determined as an intersection point of the projectile trajectory on the target surface.

Fig. 2

When the high-speed camera was used (Fig. 2c), the frame rate (10^4 frames s^{-1}) was too low to determine the projectile trajectory. We thus estimated the impact point on the target surface by using the envelope of fine fragments ejected from the impact point just after the impact. In this case, we assumed that the fine fragments were ejected in axial symmetry against the line connecting the impact point to the target center, and we were

194 able to determine the ejecta neck from the fine fragments as shown in the left image of
195 Fig. 2c. The impact point was then set at the middle point on the line linking both ejecta
196 necks.

197 We defined a head-on collision as an impact with $\theta = 80°–90°$. The impact velocity,
198 v_i, for oblique impacts was 3.8 and 6.9 km s^{-1} for the porous gypsum targets, and 4.3, 4.9,
199 and 5.9 km s^{-1} for the glass targets. For the head-on collisions, we systematically changed
200 the impact velocity from 2.2 to 6.9 km s^{-1} for both types of targets. The measured error
201 of impact velocity was ≤1%. The specific energy, Q, is usually used as a parameter
202 representing the impact condition, and it is defined by using the projectile mass, m_p, the
203 original target mass, M_t, and the impact velocity v_i as $Q \equiv \frac{1}{2} m_p {v_i}^2 / (M_t + m_p)$. For
204 the porous gypsum targets, the specific energy Q was approximately 3×10^3 and 10^4 J
205 kg^{-1} for the oblique impacts. For the glass targets, the Q was approximately 10^3, 2×10^3,
206 and 4×10^3 J kg^{-1} for the oblique impacts.

207 The target was set in an acrylic recovery box to collect the impact fragments after the
208 shot. Four of the six inside walls of the recovery box were covered with sponge plates to
209 prevent impact fragments from secondary collisions on the inside walls. The other two

210 inside walls were not covered, in order to allow observation by the high-speed camera
211 and shutter camera. The target was set in the recovery box by using strings passing
212 through a hole in the clip on the target. Most of the porous gypsum targets were suspended
213 from the top of the box (Fig. 2c). The glass targets and several porous gypsum targets
214 were set on a string net resembling a hammock (Fig. 2b). After each shot, we recovered
215 the impact fragments and measured their masses with an electrical mass balance. We
216 measured the fragments one by one to identify fragments with masses ≥0.01 g, and we
217 sieved the fragments with masses <0.01 g into four groups according to the mesh sizes of
218 the sieves: 2.0 mm, 1.4 mm, and 1.0 mm, and <1.0 mm. We measured the total mass of
219 each size group.

220 The collisional disruption of the target was observed by a high-speed camera (RX-6;
221 NAC Image Technology, Tokyo) set at the side of a vacuum chamber. The frame rate and
222 the shutter speed were set at 10^4 frames s^{-1} and 10 or 20 μs, respectively. We used a metal
223 halide lamp to illuminate the target from the side at which the camera was placed or from
224 the side behind the recovery box (Fig. 1). We used the images taken by the high-speed
225 camera for the analysis of the fragment velocity distribution, although some fragments

226 hit the strings and the velocity distribution was disturbed. We thus used only the images
227 taken during the period before fragments hit the strings for the analysis of the fragment
228 velocity distribution.
229
230 **3. Experimental Results**
231 *3.1. Observations of collisional disruption*
232 The experimental conditions and the results of each shot are summarized in Table 1 Table 1
233 for the porous gypsum targets and in Table 2 for the glass targets. Fig. 3 provides Table 2
234 snapshots of the collisional disruption of a porous gypsum target taken by the high-speed Fig. 3
235 camera impacted at the specific energies of 3×10^3 J kg^{-1} (Fig. 3a–c) and 10^4 J kg^{-1} (Fig.
236 3d–f). The impact angle θ is 75° in Fig. 3a and 3d, 45°–55° in Fig. 3b and 3e, and 10°–
237 15° in Fig. 3c and 3f. As shown in the second image in each panel, cloudy ejecta
238 composed of fine dust formed and grew as a U-shaped ejecta curtain from the impact
239 point just after the projectile impacted. At a large impact angle (75° or 45°–55°), many
240 cracks were radially generated around the impact point, and pyramid-shaped fragments
241 were ejected after 0.5–5 ms of the impact, as shown in the third to the fourth images of

Fig. 3 (panels a, b, d, and e).

At the low specific energy of 3×10^3 J kg^{-1}, large fragments formed around the antipodal point and moved slowly toward the downstream region of the projectile trajectory, and the other fragments scattered outward from the original position within 20 ms of the impact as shown in the fourth image of Fig. 3a and 3b. At the high specific energy of 10^4 J kg^{-1}, the target was disrupted catastrophically and the fragments expanded in the downstream direction (fourth images in Fig. 3d and 3e), then scattered in all directions as shown in the fifth images. In contrast, with a small impact angle (10°–15°), several large fragments were ejected from the impact point as shown in the third image in Fig. 3c and the fourth image in Fig. 3f. Within 10 to 20 ms of the impact, the largest fragment moved upward and slowly rotated counterclockwise. No cracks were observed on the surface of target for the low specific energy (Fig. 3c).

Fig. 4 presents snapshots of the glass targets at the specific energies of 10^3 J kg^{-1} and at 4×10^3 J kg^{-1}. The impact angle θ is 80° in Fig. 4a and 4d, 40°–45° in Fig. 4b and 4e, and 15° in Fig. 4c and 4f. Just after the impact (as shown in the second images), dusty fine fragments were ejected from the impact point to form an envelope resembling a pillar

Fig. 4

258 growing in the upstream direction along the line connecting the impact point with the
259 target center, and the pillar-type ejecta were quite different from the U-shaped ejecta
260 curtain formed on the porous gypsum targets. Surprisingly, fine fragments were also
261 ejected from the antipodal point, and we observed a symmetrical, cone-shaped ejecta
262 envelope around the antipodal point (Fig. 4, third images). This antipodal ejecta curtain
263 became more pronounced as the impact angle grew closer to a head-on collision. The
264 entire target was completely fractured and filled with cracks, becoming opaque (except
265 for the target at the low specific energy and $\theta = 15°$ as shown in Fig. 4c, as this glass
266 target was transparent before the shot). With the low specific energy and $\theta = 15°$, the
267 cone-type curtain did not appear at the antipodal point, but several fragments ejected. At
268 3 ms after the impact (Fig. 4, fourth images), many small but resolved fragments appeared
269 in the image and were ejected from both the impact point and the antipodal point in the
270 upstream and the downstream directions, respectively. At 20 ms after the impact (Fig. 4,
271 fifth images), the fine fragments scattered away, but the largest fragment remained at the
272 center of the image.
273

3.2. Ejecta velocity distributions of impact fragments

As noted above in Section 3.1, the impact fragments were ejected in different forms depending on the target materials. We therefore analyzed the ejecta velocity distribution depending on the initial surface position to characterize the kinetics of the impact fragments for both types of target. We did not measure individual fragment velocities directly; instead we made two types of velocity measurement. One measurement was of the expanding velocity of the ejecta envelope consisting of the fine fragments at high specific energy. The other measurement was of the ejection velocity of the impact fragments from the antipodal point (hereinafter the antipodal velocity).

The obtained high-speed images were too blurred to distinguish each fragment in the cases of the catastrophic disruption of the target, due to the hazy created by tiny fragments; it was thus difficult to trace each fragment. We therefore usually measured the expanding velocity of the ejecta envelope as a representation of the velocity of fragments ejected from the target surface at different positions. This expanding velocity was obtained by an analysis of the successive images gathered at a few milliseconds after the impact. We assumed that these tiny fragments comprising the envelope were ejected

290 radially from the impact point as in the “radial point model” proposed by *Paolicchi et al.* Fig. 5
291 [1989] and that the fragments did not have the velocity component of the line-of-sight
292 direction shown in Fig. 3d–f and Fig. 4d–f. We then defined the line connecting the target
293 center with the projectile center at the impact as the base line in order to determine the
294 initial position angle, and thereby the initial surface position, for each fragment. The base
295 line was set at 0° as shown in Fig. 5a.

296 As we assumed that the surface fragments were ejected radially from the impact point,
297 we set the impact point as the origin, and drew measurement lines from the origin at
298 successive increments of 15° (15°, 30°, etc.) from the base line (Fig. 5a). We defined the
299 region where the projectile was directed as the downstream region and set a minus (–)
300 angle. We defined the opposite region as the upstream region and set a plus (+) angle.
301 This analysis method is the same as that used by *Arakawa* [1999a].

302 Fig. 5 (panels b and c) illustrates the relationship between the expanding velocity and
303 the initial position angle for the porous gypsum and glass targets. The velocity
304 distributions of the ejecta envelope were quite different between the porous gypsum and
305 glass targets. With the porous gypsum targets, the expanding velocity grew larger as the

306 initial position angle increased in the case of a head-on collision, and the expanding
307 velocity distributions were almost axisymmetric to the initial position angle of 0°: the
308 expanding velocity became the minimum at the initial position angle of 0°. At the impact
309 angles of 20° and 55°, the expanding velocity distribution was no longer axisymmetric,
310 so that the minimum expanding velocity appeared at the initial position angle at +30°.
311 The minimum expanding velocity for each impact angle decreased from 10 m s^{-1} for the
312 head-on collision to 2 m s^{-1} for the highly oblique impact of 20°. In addition, the velocities
313 expanding in the downstream direction were higher than those expanding in the upstream
314 direction at oblique impacts.

315 These observed characteristics of expanding velocity distributions are very similar to
316 those of ice-ice oblique impacts observed by *Arakawa* [1999a]. In the present study, the
317 results of the highly oblique impact of 15° showed that the expanding velocity did not
318 depend on the initial position because the degree of disruption was not very severe, and
319 then several large fragments remained; a few fragments were measured in this case.

320 The expanding velocity distribution of the glass targets was axisymmetric to the initial
321 position angle of 0° not only for the head-on collision but also for the highly oblique

322 impacts. The expanding velocity was the maximum at the initial position angle of 0°, and
323 it decreased toward the initial position angle close to ±60°. The velocity then slightly
324 increased from 60° to 75°, irrespective of the impact angle (Fig. 5d). This slight increase
325 of the expanding velocity around 60°–75° can be simply explained by the ejecta curtain
326 formed around the impact point (as shown in the third images of Fig. 4). The expanding
327 velocity at the initial position angle of 0° increased with the increase of the impact angle,
328 but the expanding velocity at an initial position angle beyond ±30° was almost the same,
329 irrespective of the impact angle. These observed characteristics of the glass targets were
330 quite different from those of the porous gypsum targets, with the most notable difference
331 being that the expanding velocity of the glass targets was the maximum at the antipodal
332 point and rapidly decreased toward ±30°.

333 When *Gault and Wedekind* [1969] conducted impact experiments using crystal glass
334 balls at impact velocities up to 7.6 km s^{-1}, they reported that the impact fragment was
335 ejected from the antipodal point with the highest velocity among all fragments. Their
336 results were very similar to our present results using a glass target. This high expanding
337 velocity at the antipodal point could be caused by a shock wave concentration near the

338 antipodal point on the glass target surface, because the glass target in our study had a
339 perfect spherical shape with a very smooth surface and a homogeneous interior.
340 Several previous works measured the antipodal velocity as a representative velocity
341 of the low-velocity fragments for various target materials [*Fujiwara and Tsukamoto*,
342 1980; *Arakawa*, 1999a; *Okamoto and Arakawa*, 2009; *Yasui and Arakaw*a, 2011]. We
343 therefore measured the antipodal velocity, V_a, of porous gypsum and glass targets to Fig. 6
344 investigate the effects of the impact angle on the antipodal velocity. We compare the V_a
345 values of our porous gypsum targets with the values in previous studies in Fig. 6. It should
346 be noted that the minimum ejection velocity was sometimes inconsistent with the
347 antipodal velocity in the oblique impact, as discussed above.
348 Fig. 6 illustrates the relationship between the antipodal velocity V_a in the laboratory
349 coordinate system and the specific energy Q for the porous gypsum targets. The V_a for
350 the porous gypsum targets was constant for a given Q value at the impact angle θ ≥40°,
351 while at the θ ≤30°, the V_a greatly decreased with the decrease of the θ: the V_a at the
352 θ of 10° or 15° was an order of magnitude smaller than that at the θ of 90°. The V_a at
353 the impact angles ≥40° increased with the increase of the Q, and the V_a could be fitted

by a power law equation as follows:

$$V_{\mathrm{a}} = 10^{-2.21\pm0.17} Q^{0.80\pm0.04}. \quad (1)$$

Our experimental results at the impact angles ≥40° were consistent with the previous results for head-on collisions of porous gypsum targets with the porosity of 53±4%, but the previously reported values for non-porous materials such as H_2O ice and basalt were several times larger than our present findings, although the power law indices of the Q for the empirical equations in Fig. 6 were approximately 0.8, irrespective of the materials. The effect of the impact angle on the antipodal velocity is somewhat limited for porous gypsum targets; that is, the V_{a} only for highly oblique impacts with the θ <40° was several times smaller than that for the head-on collision, and the V_{a} strongly depended on the impact angle at the θ <40°.

One of the most impressive ejecta features observed on the glass targets was the abnormal high velocity fragments that jetted from the antipodal point. Fig. 7 shows the relationship between the antipodal jet velocity, V_{jet}, and the specific energy Q for the glass targets, where the V_{jet} is the expanding velocity at the antipodal point as shown in Fig. 4. The V_{jet} had an almost constant value of 182±47 m s^{-1} except for the impact angle

Fig. 7

370 of 15°, irrespective of the Q, and this velocity is much higher than the velocity of the
371 center-of-mass for each impact. The jetting mechanism at the antipodal point could be
372 very complicated related to the shock wave spreading through the target interior and
373 focusing at the antipodal point. Detailed numerical simulations may help reconstruct this
374 feature. Such detailed study is beyond the scope of the present investigation. However, a
375 simple estimate of the pressure focusing at the antipodal point, P_{a}, can be made by using
376 the V_{jet} and the Hugoniot of glass according to the equation $P_{\mathrm{a}} \approx \rho C_{\mathrm{b}} V_{\mathrm{jet}}/2$, where ρ
377 and C_{b} are the density of glass, 2,500 kg m^{-3}, and the bulk sound velocity of glass, 4 ×
378 10^3 m s^{-1} [*Melosh*, 1989]. The antipodal pressure inducing the jetting is estimated as
379 approximately 1 GPa, which is rather higher than the tensile strength of glass, 31–35 MPa
380 [*Ashby*, 2013].
381
382 *3.3. Mass frequency distribution of the recovered fragments*
383 Fig. 8 provides photographs of the recovered fragments of the porous gypsum targets. Fig. 8
384 The impact angle θ was 75° in Fig. 8a and 8d, 40°–45° in Fig. 8b and 8e, and 10°–15°
385 in Fig. 8c and 8f. The applied specific energy is ~3 × 10^3 J kg^{-1} for Fig. 8a–c and ~10^4 J

386 kg^{-1} for Fig. 8d–f. A comparison of the photos of the recovered fragments at the different
387 specific energies but a similar impact angle reveals that the degree of the impact
388 disruption is not very different, although the degree of the impact disruption changes
389 greatly with the impact angle. The targets were disrupted catastrophically at θ = 75° and
390 40°–45°, and it can be seen in Fig. 8 that the large fragments have a conical shape and/or
391 a curved surface with a black marker line, which means that they originated near the target
392 surface including the antipodal point.

393 Although core-type fragmentation is usually observed for non-porous rocky materials
394 such as basalt [*Fujiwara et al.*, 1977], we did not observe this type of fragmentation for
395 the porous gypsum targets—even with the oblique impacts— possibly because the rear-
396 surface spallation was reduced due to the strong decay of shock pressure in porous targets
397 [*Love et al.*, 1993; *Okamoto and Arakawa*, 2009]. The smaller fragments could have
398 originated mainly around the impact point, as recognized in the high-speed image in Fig.
399 3. In the case of the highly oblique impact at the θ of 10°–15°, a large crater with a
400 diameter of approximately 20 mm was observed on the target surfaces, and the crater was
401 recognized to be composed of a small pit surrounded by a spalling area.

Fig. 9

Fig. 9 shows the photographs of the recovered fragments for glass targets. The impact angle θ was 80° in Fig. 9a and 9d, 40° in Fig. 9b and 9e, and 15° in Fig. 9c and 9f. The applied specific energy was ~10^3 J kg^{-1} for Fig. 9a–c and ~4×10^3 J kg^{-1} for Fig. 9d–f. The recovered fragments of the glass targets were clearly different from those of the porous gypsum targets; i.e., the degree of the impact disruption for the glass targets changed with not only the specific energy but also the impact angle. At the low specific energy, the glass targets were partially disrupted around the impact point, and the antipodal point became truncated at both sides as shown in the expanded windows of Fig. 9a–c. In addition, many cracks were generated inside the targets so that the impacted area looked white due to the large number of small cracks.

At the large specific energy, the glass targets were disrupted catastrophically, and the size of the largest fragment became smaller as the impact angle grew larger. It was also apparent that the amount of small fragments decreased with the decrease of the impact angle. The high-speed images in Fig. 4 showed that large fragments originated from the middle part of the target, and small fragments originated around the impact point and the antipodal point. However, we did not observe core-type fragmentation for our glass

418 targets at any of the impact angles and specific energies, as was reported for basalt
419 [*Fujiwara et al.*, 1977]. The fragmentation mode of our glass targets changed directly
420 from the truncated fragmentation at low specific energy to catastrophic disruption at high
421 specific energy.

422 Fig. 10 shows the mass frequency distributions of the impact fragments at different Fig. 10
423 impact angles; they are described by the relationship between the cumulative number of
424 impact fragments, N, and the fragment mass normalized by the original target mass,
425 m/M_{t}, for porous gypsum targets at the specific energy of 3×10^3 J kg^{-1} and for glass
426 targets at the specific energy of 4×10^3 J kg^{-1}. The m/M_{t} at N=1 on the mass frequency
427 distribution indicates the largest fragment mass normalized by the original target mass,
428 $m_{\mathrm{l}}/M_{\mathrm{t}}$. In the case of the porous gypsum targets shown in Fig. 10a, the mass frequency
429 distributions obtained at the impact angle ≥45° were almost the same, and thus the mass
430 frequency distribution can be described by the same power law equation. When the
431 impact angle was changed from 45° to 10°, the amount of impact fragments was reduced
432 with the decrease of the impact angle. However, the slopes of the mass frequency
433 distribution at the m/M_{t} values smaller than 10^{-3} did not systematically depend on the

434 impact angle.

435 For the glass targets shown in Fig. 10b, the mass frequency distributions obtained for
436 the impact angles ≥40° were almost the same. When the impact angle was changed from
437 40° to 15°, the amount of impact fragments was slightly reduced within a factor of two.
438 Notably, the slope of the mass frequency distribution at the m/M_t values smaller than
439 10^{-3} was almost the same, and this is described by the power law equation, $N \propto$
440 $(m/M_t)^{-\alpha}$ [*Takagi et al.*, 1984]. The mass frequency distributions of our porous gypsum
441 and glass targets at the m/M_t values $<10^{-3}$ were fitted by the power law equation, and
442 we observed that the α values did not strongly depend on the impact angle and the
443 specific energy, as shown in Fig. 10c. Thus, the average α was 0.75±0.07 for the porous
444 gypsum targets and 0.95±0.08 for the glass targets: the α for the porous gypsum targets
445 might be smaller than that for the glass targets. These values are larger than that for
446 polycrystalline ices at 0.64±0.06 obtained by *Arakawa* [1999b], and that for basalt at
447 0.54±0.16 obtained by *Takagi et al.* [1984].

448

449 *3.4. Largest fragment mass and impact strength*

450 The largest fragment mass among all impact fragments is a good representative of the
451 degree of impact fragmentation. We thus examined the relationship between the largest
452 fragment mass normalized by the original target mass, $m_{\mathrm{l}}/M_{\mathrm{t}}$, and the impact angle θ
453 for the porous gypsum and glass targets as shown in Fig. 11, where we use the term NLFM
454 for the normalized largest fragment mass, $m_{\mathrm{l}}/M_{\mathrm{t}}$. For both types of target, the NLFM
455 was nearly constant or slightly increased with the decrease of the impact angle at the high-
456 impact angle region in all specific energies, and the NLFM values were almost the same
457 as the NLFM obtained for the head-on collision within a factor of two.

Fig. 11

458 In contrast, the NLFM increased with the decrease of the impact angle at the low-
459 impact angle region, and the NLFM rose more rapidly as the specific energy was larger.
460 It is quite clear that this quasi-constant NLFM region extended from the head-on collision
461 (θ = 90°) toward the low-impact angle region, and thus this quasi-constant region
462 continued until 30° for the porous gypsum targets and 55° for the glass targets. We defined
463 those impact angles at the boundary of the quasi-constant NLFM region as the critical
464 angle, θ_{c}, and this angle does not depend on the specific energy.

465 Generally, the NLFM has a good relationship with the specific energy for head-on

466 collisions; it is fitted by the following power law equation:

467 $$\frac{m_{\mathrm{l}}}{M_{\mathrm{t}}} = 10^{p_1} \cdot Q^{-q_1}. \qquad (2)$$

468 The impact strength, Q^*, is defined as the specific energy when the NLFM is equal to

469 0.5. Fig. 12 illustrates the relationship between the NLFM and the specific energy for the Fig. 12

470 porous gypsum targets and glass targets. For the porous gypsum targets, the NLFM at the

471 impact angle from 90° to 45° was almost the same, although it fluctuated slightly within

472 a factor of two. The NLFM at the very low impact angle clearly deviated from these high

473 impact angle data. Similarly, for the glass targets, the NLFM at the impact angle from 90°

474 to 60° was almost the same, but the NLFM at the impact angles lower than 45° was clearly

475 larger than these high impact angle data at the same Q. We observed that the glass targets

476 began to be fractured and the truncated regions appeared on both the impact and the

477 antipodal points at the specific energy of approximately 10^3 J kg^{-1}.

478 We then derived the impact strength Q^* for a head-on collision (θ of 90° and 80°),

479 and the results in Fig. 12 were thus fitted by using Eq. (2) at the NLFM values <0.75. The

480 parameters p_1 and q_1 and the obtained Q^* for the porous gypsum and glass targets are

481 summarized in Table 3. We observed that the Q^* of the porous gypsum targets was Table 3

482 slightly larger than that of the glass targets, although the static tensile strength of the
483 porous gypsum (~1 MPa from *Yasui and Arakawa* [2011]) was one order of magnitude
484 smaller than that of the glass (31–35 MPa from *Ashby* [2013]). This inconsistency
485 between the static and dynamic strength may have been caused by the low shock-induced
486 pressure and the large attenuation rate of shock pressure for porous materials [*Kawakami*
487 *et al.*, 1991]. Moreover, it is impressive that the power of Eq. (2), q_1, for glass targets
488 was approximately 2.5 times larger than that for porous gypsum targets. This means that
489 a small change of specific energy can cause a drastic change in the degree of the impact
490 fragmentation for glass targets.

491 For a comparison of our results for porous gypsum and glass targets with the findings
492 of earlier studies, the previous results for porous gypsum with a porosity of 53±4%
493 obtained by *Okamoto and Arakawa* [2009] and for basalt obtained by *Fujiwara and*
494 *Tsukamoto* [1980] are also shown in Fig. 12 and Table 3. As explained in Fig. 12, our
495 NLFM values for the porous gypsum targets were somewhat smaller than those obtained
496 by *Okamoto and Arakawa* [2009] over the range of the specific energy in the present
497 study, but the power of Eq. (2), q_1, for our porous gypsum targets was almost the same

498 as that obtained by *Okamoto and Arakawa* [2009]. When our glass targets are compared
499 with the basalt studied by *Fujiwara and Tsukamoto* [1980], it is apparent that the power
500 of Eq. (2), q_1, for our glass targets is not very different from that of basalt, and the NLFM
501 values of these two types of material were very similar, and thus the materials' impact
502 strengths were almost the same.
503
504 **4. Discussions**
505 *4.1. Effective specific energy*
506 As described above in Section 3.4., we observed that the impact strength for a head-
507 on collision was approximately 1000 J kg^{-1} for both types of target, while the NLFM
508 increased with the decrease of the impact angle at the impact angles <30° for the porous
509 gypsum targets and <55° for the glass targets. Therefore, when we determine the impact
510 strength for an impact angle smaller than these critical angles, θ_c, it can be expected to
511 be >1000 J kg^{-1}. It should thus be considered how the impact angle affects the impact
512 strength and what types of physical mechanisms control the impact strength for an oblique
513 impact. We can then reanalyze the impact strength by using the effective specific

514 energy, Q_{eff}, which is defined by the following equation:

515 $$Q_{\mathrm{eff}} = Q \sin^2 \theta = \frac{\frac{1}{2} m_{\mathrm{p}} (v_{\mathrm{i}} \sin \theta)^2}{M_{\mathrm{t}} + m_{\mathrm{p}}}. \quad (3)$$

516 The velocity component normal to the impact surface, $v_{\mathrm{i}} \sin \theta$, is only introduced into
517 the specific energy in Eq. (3) because we assume that it could induce mainly the impact
518 pressure and thereby contribute to the damage to the entire target [*Chapman and*
519 *McKinnon*, 1986; *Pierazzo and Melosh*, 2000]. We next examine the relationship between
520 the NLFM and the Q_{eff} in order to discuss the effect of the impact angle on the impact
521 strength.

522 This relationship (for both types of target) is illustrated in Fig. 13. Although the data Fig. 13
523 are slightly scattered, they were almost consistent with each other, and were fitted by one
524 empirical equation at the NLFM values <0.75, irrespective of the impact angle. However,
525 the NLFM of the glass targets behaved differently compared to that of the porous gypsum
526 targets (Fig. 13a, b). The empirical equation obtained below $m_{\mathrm{l}}/M_{\mathrm{t}}$= 0.75 for the porous
527 gypsum targets could be simply extrapolated until unity, and it was well consistent with
528 the NLFM values >0.75, whereas the two empirical equations below and above $m_{\mathrm{l}}/M_{\mathrm{t}}$=
529 0.75 for the glass targets were clearly necessary. It is clear for glass targets at $m_{\mathrm{l}}/M_{\mathrm{t}}$

>0.75 that the NLFM gradually decreased with the increase of the Q_{eff}, and the target appeared to be a sphere truncated at both the impact and antipodal points as shown in Fig. 9a–c. At $m_{\mathrm{l}}/M_{\mathrm{t}}$ <0.75, the NLFM greatly decreased with the increase of the Q_{eff}, and the target was catastrophically disrupted (Fig. 9d–f).

We can write the empirical equation representing the relationship between the NLFM and the Q_{eff} for both targets in the form of a power law equation:

$$\frac{m_{\mathrm{l}}}{M_{\mathrm{t}}} = 10^{p_2} \cdot {Q_{\mathrm{eff}}}^{-q_2}. \qquad (4)$$

The parameters p_2 and q_2 are summarized in Table 4, and we note that two empirical equations with different p_2 and q_2 values were necessary for glass targets at the NLFM values >0.75 and at those <0.75. By using these empirical equations, we were able to obtain the effective impact strength, ${Q_{\mathrm{eff}}}^*$, defined as the effective specific energy when the NLFM was equal to 0.5, and the obtained ${Q_{\mathrm{eff}}}^*$ values are also shown in Table 4. Surprisingly, the ${Q_{\mathrm{eff}}}^*$ for both targets were very similar to 1000 J kg^{-1} derived from the head-on collision. Thus, this similarity may support our assumption that the velocity component normal to the impact surface was mainly responsible for the impact pressure that damaged the entire target in the oblique impact. We can then recalculate the impact

Table 4

546 strength Q^* by using the effective impact strength $Q_{\mathrm{eff}}{}^*$ at various impact angles, since
547 the results of our experiments confirmed that $Q_{\mathrm{eff}}{}^*$ can be written as $Q^* \sin^2 \theta$.

548 The results of the porous gypsum and glass targets are shown together in Fig. 13c. It
549 can be easily seen that the NLFM for the porous gypsum targets was always larger than
550 that for the glass targets over the range of Q_{eff} explored in these experiments, and the
551 NLFM of both targets crossed at Q_{eff} = 750 J kg^{-1} and $m_{\mathrm{l}}/M_{\mathrm{t}}$ = 0.69. The results for
552 basalt obtained by *Fujiwara and Tsukamoto* [1980] are also shown in Fig. 13c; they
553 carried out impact experiments for a basalt sphere or cube at impact angles from 90° to
554 30° and the impact velocity of approximately 2.7 km s^{-1}. The parameters p_2 and q_2 and
555 the effective impact strength $Q_{\mathrm{eff}}{}^*$ of their basalt targets are also shown in Table 4 for a
556 comparison with our findings. The NLFM of basalt was well consistent with that of our
557 glass targets.

558 To test whether the empirical equation, Eq. (4), can reproduce the relationship
559 between the NLFM and the impact angle θ, we prepared Fig. 14 illustrating the
560 relationship between the NLFM and the $\sin\theta$ values and replotted our data in the figure.
561 Equation (4) with the p_2 and q_2 data shown in Table 4 was then drawn. It was thus

Fig. 14

562 clear that Eq. (4) could reproduce our experimental results very well for both types of
563 targets, although the glass target results were slightly scattered for 1000 J kg^{-1} and at the
564 $\sin\theta$ values >0.8, as shown in Fig. 14b.

565 We reanalyzed the antipodal velocity, V_a, for the porous gypsum targets by using the
566 Q_{eff} to examine the effects of the impact angle on the V_a. This relationship is illustrated Fig. 15
567 in Fig. 15a. As with the NLFM results, the V_a results were well merged and fitted by the
568 following empirical equation:

569 $$V_a = 10^{-1.72\pm0.10} {Q_{eff}}^{0.68\pm0.03}. \quad (5)$$

570 As shown in Fig. 15b, we were also able to reproduce the relationship between the V_a
571 and the specific energy for porous gypsum targets by using Eq. (5), and the data shown
572 in Fig. 6 were also replotted. The use of Eq. (5) clearly reproduced our experimental
573 results very well, as with the results of Fig. 14. We were thus also able to recalculate the
574 antipodal velocity V_a by using Eq. (5) at various impact angles.

575

576 *4.2. Implications for the probability of impact disruption considering oblique impacts*

577 Our findings clarified that the degree of disruption represented by the NLFM depends

578 on the impact angle for porous gypsum and glass targets, as described in Eq. (4). The
579 probability of an impact at an impact angle between θ and $\theta + d\theta$ is described as
580 $dP = 2 \sin\theta \cos\theta \, d\theta$ according to *Shoemaker* [1962] and *Pierazzo and Melosh* [2000],
581 irrespective of the target body's gravity. In the following discussion, therefore, we will
582 consider the effects of the probability of oblique impacts on the degree of disruption in
583 the solar nebula, and we speculate that (1) primitive rocky planetesimals could be
584 represented by our porous gypsum targets, and (2) consolidated rocky planetesimals could
585 be represented by our glass targets.

586 The probability density function for oblique impacts is expressed as:

587 $$\frac{dP}{d\theta} = 2 \sin\theta \cos\theta, \qquad (6)$$

588 and this function has the maximum at $\theta = 45°$. By using Eqs. (3), (4), and (6), we can
589 obtain the relationship between the probability density function, $dP/d\theta$, and the
590 normalized largest fragment mass (NLFM), $m_{\mathrm{l}}/M_{\mathrm{t}}$, as follows:

591 $$\frac{dP}{d\theta} = 2\left[k^{-1}\left(\frac{2m_{\mathrm{l}}}{M_{\mathrm{t}}}\right)^{-\frac{1}{q_2}}\left\{1 - k^{-1}\left(\frac{2m_{\mathrm{l}}}{M_{\mathrm{t}}}\right)^{-\frac{1}{q_2}}\right\}\right]^{\frac{1}{2}}, \qquad (7)$$

592 where k represents the specific energy normalized by the impact strength, Q/Q^*, and
593 $Q_{\mathrm{eff}}{}^*$ was assumed to be equal to Q^* based on our present findings. The detailed

derivation process considered by Eq. (7) is explained in the Appendix. The relationship between the $dP/d\theta$ and the NLFM can be calculated at various specific energies in Eq. (7), and it can then be estimated how oblique impacts in the solar nebula affected the NLFM, because it was clear according to Eq. (6) that almost no head-on collisions occurred; a specific energy larger than Q^* was therefore necessary to cause a catastrophic disruption in the planetary collisional processes considering the oblique impacts.

Fig. 16a shows the relationship between the $dP/d\theta$ and m_l/M_t data for primitive rocky planetesimals simulated by porous gypsum. The function is calculated for the normalized specific energy of $k = 3$ ($Q^* = 1.33 \times 10^3$ J kg^{-1} and $q_2 = 0.76$). The $dP/d\theta$ increases with increasing m_l/M_t, reaches a maximum of $dP/d\theta = 1$ at $m_l/M_t = 0.37$, and then decreases with increasing m_l/M_t to become $dP/d\theta = 0.68$ at $m_l/M_t = 1$. The numbers added to the function of $dP/d\theta$ show the impact angle corresponding to each m_l/M_t, and the results demonstrate that the probability density function is 0 at $\theta = 90°$ and 1 (the maximum) at $\theta = 45°$. Moreover, the m_l/M_t is 1 at the θ of 21.5°; this means that the planetesimals were almost intact when they were

Fig. 16

610 impacted at an impact angle ≤21.5°.

611 The cumulative distribution function, $P(<\theta)$, is also shown in Fig. 16a. We define
612 the $P(<\theta)$ as the impact probability, i.e., it indicates the probability of impact at an
613 impact angle smaller than a specific impact angle θ. The $P(<\theta)$ can be obtained by
614 integrating Eq. (7) with respect to the impact angle θ from 0° to a specific θ, and the
615 $m_{\mathrm{l}}/M_{\mathrm{t}}$ corresponding to each impact angle is calculated by using Eqs. (3) and (4) at
616 constant k; the relationship between $P(<\theta)$ and $m_{\mathrm{l}}/M_{\mathrm{t}}$ is then derived as shown in
617 Fig. 16a. It is observed that the $m_{\mathrm{l}}/M_{\mathrm{t}}$ is ≥0.37 with a probability of 50%, and the
618 planetesimals are almost intact with a probability of 14%.

619 Fig. 16b shows the impact probability for primitive and consolidated rocky
620 planetesimals, which were calculated for the normalized specific energy k of 0.7, 1, 3,
621 and 10. We used the parameters of porous gypsum and glass targets listed in Table 4 to
622 calculate these values. In both planetesimals, the $m_{\mathrm{l}}/M_{\mathrm{t}}$ becomes smaller with the
623 increase of the normalized specific energy at the same impact probability. It was also
624 shown that at $m_{\mathrm{l}}/M_{\mathrm{t}} = 1$, the impact probability corresponding to keeping planetesimals
625 intact after the collision decreases with the increase of the normalized specific energy. In

626 comparison of the results of the primitive rocky planetesimals with those of the
627 consolidated planetesimals, the degree of disruption (m_l/M_t) for the consolidated rocky
628 planetesimals fluctuated approximately four times at the impact probability between the
629 head-on collision ($P = 1$) and the oblique impact of 45° ($P = 0.5$), whereas the m_l/M_t
630 of the primitive rocky planetesimals was almost constant within the same impact
631 probability range.

632 At the same normalized specific energy, the impact probability of the primitive rocky
633 planetesimals for m_l/M_t <0.5 is always larger than that of the consolidated rocky
634 planetesimals. For example, at the normalized specific energy of 10, the impact
635 probability of the primitive rocky planetesimals for m_l/M_t >0.1 is 0.83 (θ ~66°) and
636 that of the consolidated rocky planetesimals is 0.27 (θ ~31°). Thus there is a more than
637 threefold difference in the impact probability between them. As a result, the consolidated
638 rocky planetesimals can be more easily disrupted into small fragments compared to the
639 primitive rocky planetesimals.

640 In contrast, the impact probability of the consolidated rocky planetesimals is larger
641 than that of the primitive rocky planetesimals for m_l/M_t >0.5 at the same k. It is also

642 notable that the impact probability for both planetesimals crosses at $m_l/M_t = 0.5$ when
643 the k is the same. In this case, the impact angle can be determined by using the following
644 equation, $\theta_{CD} = \arcsin(k^{-1/2})$, from $Q_{eff} = Q\sin^2\theta$ and the assumption of $Q_{eff}{}^* =$
645 Q^*. That is, the impact angle at which the catastrophic disruption could begin to occur,
646 θ_{CD}, is independent of the target material, but it depends only on the specific energy
647 normalized by the impact strength. At a θ larger than the θ_{CD}, the target body could be
648 disrupted catastrophically, and we can thus calculate the range of the θ necessary for
649 catastrophic disruption at each k.

650 According to this θ range, we can also calculate the impact probability of rocky
651 planetesimals at catastrophic disruption in the solar nebula by using Eq. (6), as $P(>\theta) =$
652 $1 - k^{-1}$. Fig. 16c describes the relationship between the impact probability $P(>\theta)$
653 corresponding to the occurrence of catastrophic disruption, and the normalized specific
654 energy k. The impact probability $P(>\theta)$ at the NLFM <0.5 increased with the increase
655 of the k, and it was closer to unity at large k values. That is, the catastrophic disruption
656 could occur even at a low impact angle as the normalized specific energy increases. For
657 example, to be necessary for catastrophic disruption with a probability of 50% (θ =90°–

45°), $k = 2$ is proposed, and for a probability of 75% (θ =90°–30°), $k = 4$ is proposed. We can therefore say that the catastrophic disruption could have occurred at a wide range of impact angles when the specific energy at the collision was approximately four times larger than the impact strength.

The effects of oblique impacts described in this study should thus be considered in order to construct the appropriate numerical model for the study of the mass frequency distributions of planetesimals and asteroids.

In this study, we examined the collisional disruption of solid materials in a strength-dominated regime. Our experimental results can be applied to mutual collisions of bodies with a radius <100 m in a strength regime [*Holsapple et al.*, 2002]. However, to apply our experimental results to the collisional disruption of asteroids and planetesimals >100 m, the effect of the bodies' self-gravity on the re-accumulation processes of impact fragments should be considered. In this study, we provide the basic data of the ejecta velocity distribution and the mass distributions of impact fragments that are necessary for the study of re-accumulation processes of the bodies. Numerical simulations referring to our experimental results are expected in the future.

674

675 **5. Summary**

676 We carried out oblique high-velocity impact experiments using porous gypsum and
677 glass spheres at impact angles from 90° (a head-on collision) to 10° (a grazing collision)
678 and at impact velocities from 7 to 2 km s^{-1}. We then examined the effects of the impact
679 angle on the ejection velocity of the impact fragments and the impact strength. Our results
680 are summarized as follows:

681 (1) The expanding velocity of the ejecta envelope was measured. At the initial position
682 angle of 0° (the antipodal point), the expanding velocity became the minimum at a
683 head-on collision for the porous gypsum targets. As the impact angle decreased, the
684 initial position angle where the expanding velocity showed the minimum changed
685 from 0° to +30° . For the glass targets, in contrast, the expanding velocity reached the
686 maximum at the initial position angle of 0°, irrespective of the impact angle.

687 (2) When the Q was constant, the NLFM, m_l/M_t, was almost the same at the large
688 impact angle, whereas it rose markedly with the decrease of the impact angle at θ
689 values smaller than 30° and 55° for the porous gypsum and glass targets, respectively.

690 The impact strength Q^* values for the porous gypsum and glass targets at a head-on
691 collision were obtained to be 1330 and 1070 J kg^{-1}, but compared to the porous
692 gypsum targets, the glass targets were disrupted more catastrophically with a small
693 change of the specific energy.
694 (3) We defined the effective specific energy, $Q_{\rm eff}$ ($= Q \sin^2 \theta$), and observed that the
695 NLFM, $m_{\rm l}/M_{\rm t}$, had a good correlation with the $Q_{\rm eff}$ irrespective of the impact angle.
696 At the $m_{\rm l}/M_{\rm t}$ values <0.75, the relationship can be written as $m_{\rm l}/M_{\rm t} = 10^{2.02\pm0.22} \cdot$
697 ${Q_{\rm eff}}^{-0.76\pm0.06}$ for the porous gypsum targets and $m_{\rm l}/M_{\rm t} = 10^{4.66\pm0.39} \cdot$
698 ${Q_{\rm eff}}^{-1.68\pm0.12}$ for the glass targets. The effective impact strength ${Q_{\rm eff}}^*$, i.e., the $Q_{\rm eff}$
699 at $m_{\rm l}/M_{\rm t}$ =0.5, was surprisingly consistent for both types of target at ~1000 J kg^{-1}.
700 The relationship between the antipodal velocity for the porous gypsum targets $V_{\rm a}$ and
701 the $Q_{\rm eff}$ was obtained as $V_{\rm a} = 10^{-1.72\pm0.10} {Q_{\rm eff}}^{0.68\pm0.03}$.
702 (4) We estimated the relationship between the impact probability and the NLFM, $m_{\rm l}/M_{\rm t}$,
703 by using our empirical equations. At the $m_{\rm l}/M_{\rm t}$ <0.5, the impact probability of
704 consolidated rocky planetesimals simulated by glass targets was always smaller than
705 that of primitive rocky planetesimals simulated by porous gypsum targets at a constant

706 normalized specific energy Q/Q^*, while these results were the opposite at the m_l/M_t

707 >0.5. Our findings also clarified that catastrophic disruption can occur at an impact

708 angle from 30° to 90° irrespective of the target materials when the specific energy at

709 the collision is approximately four times larger than the impact strength.

Appendix

The probability density function of impacting bodies, $dP/d\theta$, shown by Eq. (6) can be rearranged as

$$\frac{dP}{d\theta} = 2\sin\theta\cos\theta = 2\sin\theta\,(1-\sin^2\theta)^{\frac{1}{2}}, \qquad \text{(A1)}$$

by using the fundamental Pythagorean trigonometric identity.

By using Eqs. (3) and (4), we can obtain the relationship between the specific energy Q and $\sin\theta$ as follows:

$$\sin\theta = \left[\frac{1}{Q}\left\{\frac{1}{A'}\left(\frac{m_{\mathrm{l}}}{M_{\mathrm{t}}}\right)\right\}^{-\frac{1}{q_2}}\right]^{\frac{1}{2}}, \qquad \text{(A2)}$$

where $A' = 10^{p_2}$. Thus, substituting Eq. (A2) for Eq. (A1), we have

$$\frac{dP}{d\theta} = 2\left[\frac{1}{Q}\left\{\frac{1}{A'}\left(\frac{m_{\mathrm{l}}}{M_{\mathrm{t}}}\right)\right\}^{-\frac{1}{q_2}}\right]^{\frac{1}{2}}\left(1-\left[\frac{1}{Q}\left\{\frac{1}{A'}\left(\frac{m_{\mathrm{l}}}{M_{\mathrm{t}}}\right)\right\}^{-\frac{1}{q_2}}\right]\right)^{\frac{1}{2}}. \qquad \text{(A3)}$$

Here, we assumed that the effective impact strength $Q_{\mathrm{eff}}{}^{*}$ was equal to the impact strength Q^{*} when the NLFM was 0.5, as described in Section 4.2. We can thus obtain the Q^{*} by using Eq. (4) as follows:

$$\left(\frac{1}{A'}\right)^{-\frac{1}{q_2}} = 2^{-\frac{1}{q_2}}\cdot Q^{*}. \qquad \text{(A4)}$$

Thus, substituting Eq. (A4) for Eq. (A3), we can obtain Eq. (7).

Acknowledgements

We appreciate the assistance of Dr. K. Ogawa and Dr. C. Okamoto of Kobe University in the conduct of these experiments. We also thank Mr. K. Sangen of Kobe University for his technical help. Our series of our experiments were supported in part by the Center of Planetary Science at Kobe University and the Hypervelocity Impact Facility at ISAS/JAXA. This work was supported in part by a Grant-in-Aid for Scientific Research (no. 16H04041) from the Japan Ministry of Education, Culture, Sports, Science and Technology.

References

Arakawa, M., 1999a. Ejection velocities of ice fragments in oblique impacts of ice spheres. Adv. Space Res. 23, 1217–1224.

Arakawa, M., 1999b. Collisional disruption of ice by high-velocity impact. Icarus 142, 34–45.

Arakawa, M., Leliwa-Kopystynski, J., Maeno, N., 2002. Impact experiments on porous icy-silicate cylindrical blocks and the implication for disruption and accumulation of

741 small icy bodies. Icarus 158, 516–531.

742 Ashby, M. F., 2013. Material profiles. In: Materials and the Environment 2nd Edition,

743 Elsevier, pp. 459–595.

744 Asphaug, E., Ryan, E. V., Zuber, M. T., 2002. Asteroid interiors. In: Asteroids III, Eds:

745 Bottke, W. F., Cellino, A., Paolicchi, P., Binzel, R., Univ. Arizona Press, Tucson, pp.

746 463–484.

747 Chapman, C. R., McKinnon, W. B., 1986. Cratering of planetary satellites. In *Satellites,*

748 eds: J. A. Burns, M. S. Matthews, Univ. Arizona Press, Tucson, pp. 492–580.

749 Fujii, Y., Nakamura, A. M., 2009. Compaction and fragmentation of porous gypsum

750 targets from low-velocity impacts. Icarus 201, 795–801.

751 Fujiwara, A., Kamimoto, G., Tsukamoto, A., 1977. Destruction of basaltic bodies by

752 high-velocity impact. Icarus 31, 277–288.

753 Fujiwara, A., Tsukamoto, A., 1980. Experimental study on the velocity of fragments in

754 collisional breakup. Icarus 44, 142–153.

755 Gault, D. E., Wedekind. J. A., 1969. The destruction of tektites by micrometeoroid impact.

756 J. Geophys. Res. 74, 6780–6794.

757 Genda, H., Fujita, T., Kobayashi, H., Tanaka, H., Suetsugu, R., Abe, Y., 2017. Impact
758 erosion model for gravity-dominated planetesimals. Icarus 294, 234–246.
759 Heißelmann, D., Blum, J., Fraser, H. J., and Wolling, K., 2010. Microgravity experiments
760 on the collisional behavior of saturnian ring particles. Icarus 206, 424–430.
761 Henke, S., Gail, H.-P., Trieloff, M., Schwarz, W. H., Kleine, T., 2012. Thermal evolution
762 and sintering of chondritic planetesimals. Astron. Astrophys. 537, A45.
763 Holsapple, K. A., Giblin, I., Housen, K. R., Nakamura, A., Ryan, E., 2002. Asteroid
764 impacts: Laboratory experiments and scaling laws. In Asteroids III, eds: W. F. Bottke
765 Jr., A. Cellino, P. Paolicchi, R. P. Binzel, Univ. Arizona Press, Tucson, pp. 443–462.
766 Kadono, T., Arakawa, M., Ito, T., Ohtsuki, K., 2009. Spin rates of fast-rotating asteroids
767 and fragments in impact disruption. Icarus 200, 694–697.
768 Kawakami, S., Mizutani, H., Takagi, Y., Kato, M., Kumazawa, M., 1983. Impact
769 experiments on ice. J. Geophys. Res. 88, 5806–5814.
770 Kawakami, S., Kanaori, Y., Fujiwara, A., Arakawa, M., Kato, M., Mizutani, H., Cerroni,
771 P., Capaccioni, F., 1991. An experimental study of impact fracturing of small
772 planetary bodies in the solar system with an application to Phobos. Astronom.

773 Astophys. 241, 233–242.

774 Leinhardt, Z. M., Richardson, D. C., 2002. *N*-Body simulations of planetesimal evolution:

775 Effect of varying impactor mass ratio. Icarus 159, 306–313.

776 Lichtenberg, T., Golabek, G. J., Gerya, T. V., Meyer, M. R., 2016. The effects of short-

777 lived radionuclides and porosity on the early thermo-mechanical evolution of

778 planetesimals. Icarus 274, 350–365.

779 Love, S. G., Hörz, F., Brownlee, D. E., 1993. Target porosity effects in impact cratering

780 and collisional disruption. Icarus 105, 216–224.

781 Melosh, H. J., 1989. Impact cratering. Oxford Univ. Press, New York, pp. 245.

782 Morris, A. J. W., Burchell, M. J., 2017. Laboratory tests of catastrophic disruption of

783 rotating bodies. Icarus 296, 1–98.

784 Movshovitz, N., Nimmo, F., Korycansky, D. G., Asphaug, E., Owen, J. M., 2016. Impact

785 disruption of gravity-dominated bodies: New simulation data and scaling. Icarus 275,

786 85–96.

787 Nakamura, A. M., 1993. Laboratory studies on the velocity of fragments from impact

788 disruptions. The institute of Space and Astronautical Science Report, No. 651, ISSN

789 0285–6808.

790 Nakamura, A. M., Hiraoka, K., Yamashita, Y., Machii, N., 2009. Collisional disruption

791 experiments of porous targets. Planet. Space Sci. 57, 111–118.

792 Neumann, W., Breuer, D., Spohn, T., 2012. Differentiation and core formation in

793 accreting planetesimals. Astron. Astrophys. 543, A141.

794 Okamoto, C., Arakawa, M., 2009. Experimental study on the collisional disruption of

795 porous gypsum spheres. Meteorit. Planet. Sci. 44, 1947–1954.

796 Onose, N., Fujiwara, A., 2004. Mass-velocity distributions of fragments in oblique impact

797 cratering on gypsum. Meteorit. Planet. Sci. 39, 321–331.

798 Paolicchi, P., Cellino, A., Farinella, P., Zappala, V., 1989. A semiempirical model of

799 catastrophic breakup processes. Icarus 77, 187–212.

800 Pierazzo, E., Melosh, H. J., 2000. Understanding oblique impacts from experiments,

801 observations, and modeling. Annu. Rev. Earth Planet. Sci. 28, 141–167.

802 Shoemaker, E. M., 1962. Interpretation of lunar craters. In: Kopal, Z. (Ed.), Physics and

803 astronomy of the Moon. New York: Academic Press, pp. 283–359.

804 Sierks H. et al., 2011. Images of Asteroid 21 Lutetia: A remnant planetesimal from the

early solar system. Science 334, 487–490.

Takagi, Y., Mizutani, H., Kawakami, S., 1984. Impact fragmentation experiments of basalts and pyrophyllites. Icarus 59, 462–477.

Weidenschilling, S. J., 1994. Origin of cometary nuclei as ‘rubble piles’. Nature 368, 721–723.

Weidenschilling, S. J., 2011. Initial sizes of planetesimals and accretion of the asteroids. Icarus 214, 671–684.

Yasui, M., Arakawa, M., 2011. Impact experiments of porous gypsum-glass bead mixtures simulating parent bodies of ordinary chondrites: Implications for re-accumulation processes related to rubble-pile formation. Icarus 214, 754–765.

Yasui, M., Arakawa, M., Hasegawa, S., Fujita, Y., Kadono, T., 2012. In situ flash X-ray observation of projectile penetration processes and crater cavity growth in porous gypsum target analogous to low-density asteroids. Icarus 221, 646–657.

818 **Figure Captions**

819

820 **Figure 1:**

821 Top view of the two-stage light gas gun and experimental setup. The small panel at upper

822 right provides a side view of the recovery box.

823

824 **Figure 2:**

825 The analysis method used to determine the impact angle, θ. (a) Definition of the θ. (b)

826 Example of the θ determined by using the images taken by a shutter camera. Left images

827 were taken at 5 and 12 μs before the impact. Right image is the superimposed image by

828 using two images on the left. (c) Example of the θ determined by using the images taken

829 by a high-speed camera. The images are the identical, but some notes are added on the

830 right image to determine the impact angle. The impact point was determined as the middle

831 point on the line linking both ejecta necks.

832

833 **Figure 3:**

834 Snapshots of the porous gypsum targets taken by the high-speed camera. The run number
835 and the impact angle in each panel were as follows. (a) 20141208-1, θ=75°. (b)
836 20141209-2, θ=45°. (c) 20150515-1, θ=10°. (d) 20150515-2, θ=90°. (e) 20150515-
837 3, θ=55°. (f) 20151119-3, θ=15°. The specific energy in each figure was 3×10^3 J kg^{-1}
838 in (a–c) and 10^4 J kg^{-1} in (d–f). The black circle represents the projectile and the arrow
839 represents the projectile trajectory. The black bar shown on each panel represents a length
840 of 10 mm. The number shown on the right of each image represents the elapsed time after
841 the impact in ms, and "0 ms" indicates the moment of impact.
842
843 **Figure 4:**
844 Snapshots of the glass targets taken by the high-speed camera. The run number and the
845 impact angle in each panel were as follows. (a) 20151007-1, θ=80°. (b) 20151008-2,
846 θ=45°. (c) 20151125-1, θ=15°. (d) 20151001-1, θ=80°. (e) 20151118-1, θ=40°. (f)
847 20151202-1, θ=15°. The specific energy in each figure was 10^3 J kg^{-1} in (a–c) and $4 \times$
848 10^3 J kg^{-1} in (d–f). The black circle represents the projectile and the arrow represents the
849 projectile trajectory. The black bar shown on each panel represents a length of 10 mm.

The number shown on the right of each image represents the elapsed time after the impact in ms, and "0 ms" indicates the moment of impact. The fifth image on panel (c) was taken at 15 ms after the impact.

Figure 5:

(a) Schematic illustration of the definition of the initial position angle. (b) Relationship between the expanding velocity of the ejecta envelope and the initial position angle for the porous gypsum targets at the specific energy of 10^4 J kg^{-1}. The run numbers of all data are shown in Table 1. The numbers in the legend indicate the measured impact angle and those in parentheses indicate the impact angle used in the text. (c) Relationship between the expanding velocity and the initial position angle for the glass targets at the specific energy of 4×10^3 J kg^{-1}. The run numbers of all data are shown in Table 2. (d) The enlarged part of the vertical axis in panel (c) ranging from 0 m s^{-1} to 50 m s^{-1}. The error bars on panels (b) – (d) were smaller than the symbol's size.

Figure 6:

866 Relationship between the antipodal velocity V_a and the specific energy Q for the porous
867 gypsum targets. Each symbol represents the impact angle. The dashed thick line
868 represents the fitting line determined by using the power law equation of Eq. (1). Four
869 thin lines show the results for H_2O ice, basalt, and porous gypsum obtained in previous
870 works. The numbers in the parentheses indicate the impact angle: "ice" obtained by
871 *Arakawa* [1999a], "basalt" by *Fujiwara and Tsukamoto* [1980], and "gypsum" by
872 *Okamoto and Arakawa* [2009].
873
874 **Figure 7:**
875 Relationship between the antipodal jet velocity V_{jet} and the specific energy Q for the
876 glass targets. The symbols represent different impact angles.
877
878 **Figure 8:**
879 Photographs of the recovered impact fragments of the porous gypsum targets at the
880 specific energy of 3×10^3 J kg^{-1} in (a–c) and at 10^4 J kg^{-1} in (d–f). The run number and
881 the impact angle in each panel were as follows. (a) 20141208-1, θ=75°. (b) 20141209-2,

882 θ=45°. (c) 20150515-1, θ=10°. (d) 20141209-5, θ=75°. (e) 20141209-7, θ=40°. (f)

883 20150722-1, θ=15°. ”LF” surrounded by the white dashed line was the largest fragment.

884 The fragment shown on panels (c) and (f) is the largest.

885

886 **Figure 9:**

887 Photographs of the recovered impact fragments of the glass targets at the specific energy

888 of 10^3 J kg^{-1} in (a–c) and at 4×10^4 J kg^{-1} in (d–f). The run number and the impact angle

889 in each panel were as follows. (a) 20151007-1, θ=80°. (b) 20151028-2, θ=40°. (c)

890 20151125-1, θ=15°. (d) 20151001-1, θ=80°. (e) 20151118-1, θ=40°. (f) 20151202-1,

891 θ=15°. ”LF” surrounded by the white dashed line was the largest fragment. The small

892 boxes in (a–c) are expanded images of the largest fragment in each panel.

893

894 **Figure 10:**

895 Mass frequency distributions of recovered impact fragments for (a) the porous gypsum

896 targets at the specific energy of 3×10^3 J kg^{-1} and (b) the glass targets at the specific

897 energy of 4×10^3 J kg^{-1}. Each symbol represents the impact angle. The numbers in the

898 legend indicate the measured impact angle. The numbers in parentheses indicate the
899 impact angle used in the text. (c) Relationship between the power law index α in the
900 power law equation showing the mass frequency distribution of impact fragments and the
901 impact angle. The solid line and dashed line show the average values of α for the porous
902 gypsum and glass targets, respectively.
903
904 **Figure 11:**
905 Relationship between the largest fragment mass normalized by the original target mass
906 (NLFM), $m_{\mathrm{l}}/M_{\mathrm{t}}$, and the impact angle θ for (a) the porous gypsum targets and (b) the
907 glass targets. The numbers in the legend represent the target diameter and the impact
908 velocity. The numbers in the parentheses indicate the specific energy. The dashed line
909 indicates the critical impact angle of the quasi-constant NLFM, θ_{c}.
910
911 **Figure 12:**
912 Relationship between the largest fragment mass normalized by the original target mass
913 (NLFM), $m_{\mathrm{l}}/M_{\mathrm{t}}$, and the specific energy Q for (a) the porous gypsum targets and (b)

914 the glass targets. Each symbol represents the impact angle. The solid line shows the fitting
915 line determined by using the power law equation of Eq. (2) at the impact angle of 90° and
916 80°. The dotted line indicates the previous results for porous gypsum obtained by
917 *Okamoto and Arakawa* [2009] shown as "O&A [2009]" on panel (a) and for basalt
918 obtained by *Fujiwara and Tsukamoto* [1980] shown as "F&T [1980]" on panel (b).
919
920 **Figure 13:**
921 Relationship between the largest fragment mass normalized by the original target mass
922 (NLFM), $m_{\mathrm{l}}/M_{\mathrm{t}}$, and the effective specific energy Q_{eff} defined by Eq. (3), for (a) the
923 porous gypsum targets and (b) the glass targets. Each symbol represents the impact angle.
924 The solid line shows the fitting line determined by using the power law equation of Eq.
925 (4). (c) The merged figure of panels (a) and (b) and the previous results for basalt obtained
926 by *Fujiwara and Tsukamoto* [1980] shown as "F&T, 1980". Three lines show the fitting
927 lines determined by using Eq. (4).
928
929 **Figure 14:**

930 Relationship between the largest fragment mass normalized by the original target mass
931 (NLFM), m_l/M_t, and the $\sin\theta$ (the θ is the impact angle) for (a) the porous gypsum
932 targets and (b) the glass targets. Each symbol represents the experimental results, and the
933 numbers in the legend represent the target diameter and the impact velocity. The thick
934 lines show the calculated results from Eq. (4) with the obtained parameters in Table 4 at
935 each specific energy.
936
937 **Figure 15:**
938 (a) Relationship between the antipodal velocity V_a and the effective specific energy Q_{eff}
939 for the porous gypsum targets. Each symbol represents the impact angle. The thick solid
940 line shows the fitting line determined by using the power law equation of Eq. (5). (b)
941 Relationship between the antipodal velocity V_a and the specific energy Q. The data
942 plotted in this figure are identical to those in Fig. 6. The thick solid line shows the fitting
943 line by using Eq. (1). The thin lines show the calculated results from Eq. (5) at impact
944 angles of 45° (short dashed line), 30° (long dashed line), 20° (thin solid line), and 15°
945 (dotted line).

946

947 **Figure 16:**

948 (a) Relationship between the probability density function of an impact, $dP/d\theta$ (solid
949 line) on the left vertical axis, or the impact probability, $P\ (<\theta)$ (thick dotted line) on
950 the right vertical axis, and the normalized largest fragment mass (NLFM), $m_{\rm l}/M_{\rm t}$, for a
951 primitive planetesimal simulated by porous gypsum at the specific energy normalized by
952 the impact strength Q/Q^* of 3. The number on the solid line shows the impact angle θ
953 corresponding to each NLFM. The two circle symbols on the thick dotted line show the
954 data at $P = 0.5$ and $\theta = 45°$, and that at $P = 0.14$ and $m_{\rm l}/M_{\rm t} = 1$. (b) Relationship
955 between the impact probability $P\ (<\theta)$ and the NLFM, $m_{\rm l}/M_{\rm t}$, at the normalized
956 specific energy $Q/Q^*\ (=k)$ of 0.7, 1, 3, and 10 for a primitive planetesimal and a
957 consolidated planetesimal simulated by porous gypsum and glass, respectively. The solid
958 grey line indicates $m_{\rm l}/M_{\rm t}$ =0.5. The two circles show the data at $P = 0.83$ on the thin
959 dashed line (primitive planetesimal) and $P = 0.27$ on the thick dashed line (consolidated
960 planetesimal) at $m_{\rm l}/M_{\rm t} = 0.1$ and $k = 10$. (c) Relationship between the impact
961 probability $P(>\theta)$, corresponding to the occurrence of catastrophic disruption (the

962 NLFM, m_l/M_t <0.5), and the k. The number near each circle on the line shows the

963 impact angle θ corresponding to each k.

964 **Table 1.** Experimental conditions and results for porous gypsum targets

Run number [a]	Target			Impact velocity v_i, km s^{-1}	Impact angle θ[b], degree	Specific energy Q, J kg^{-1}	NLFM m_l/M_t[c]	Antipodal velocity V_a[d], m s^{-1}	α[e]
	Mass M_t, g	Diameter, mm	Porosity, %						
Oblique impact: Target diameter = 70 mm, Impact velocity ~3.8 km s^{-1}									
20141208-1$^+$	180.3	70.1	54	3.66	77.8 (75)	2.51 x 10^3	0.341	3.27 (0.09)	0.58 (0.02)
20141208-2	171.1	69.8	56	3.73	74.9 (75)	2.76 x 10^3	0.283	3.14 (0.09)	0.67 (0.03)
20141209-1	161.3	69.1	58	3.74	53.7 (55)	2.94 x 10^3	0.415	2.67 (0.06)	0.72 (0.01)
20141209-2$^+$	171.4	69.3	55	3.80	43.4 (45)	2.86 x 10^3	0.417	2.37 (0.04)	0.68 (0.02)
20141209-3$^+$	174.8	69.8	55	3.74	27.6 (30)	2.71 x 10^3	0.865	1.40 (0.02)	0.77 (0.03)
20150114-3	150.5	69.9	62	3.78	12.0 (10)	3.22 x 10^3	0.997	–	0.80 (0.05)
20150515-1$^+$	162.8	70.1	59	3.78	9.2 (10)	2.98 x 10^3	0.994	0.43 (0.01)	0.76 (0.09)
Oblique impact: Target diameter = 50 mm, Impact velocity ~3.8 km s^{-1}									
20150515-3*	50.5	48.9	63	3.76	55.9 (55)	9.49 x 10^3	0.144	9.86 (0.04)	0.86 (0.01)
20150515-4*	48.9	49.3	64	3.84	21.5 (20)	1.02 x 10^4	0.205	4.55(0.09)	0.87 (0.01)
20151119-3*	53.4	48.5	59	4.07	14.9 (15)	1.05 x 10^4	0.582	1.78 (0.03)	–
Oblique impact: Target diameter = 70 mm, Impact velocity ~6.9 km s^{-1}									
20141209-5	174.6	70.1	56	6.94	78.0 (75)	9.36 x 10^3	0.116	7.74 (0.08)	0.71 (0.01)
20141209-6	176.7	69.6	55	6.98	58.8 (60)	9.35 x 10^3	0.214	7.87 (0.12)	0.65 (0.01)
20141209-7	177.8	69.4	54	6.88	41.4 (40)	9.03 x 10^3	0.221	7.22 (0.23)	0.71 (0.01)
20150721-1	175.5	69.2	54	6.91	42.0 (40)	9.25 x 10^3	0.276	–	0.78 (0.02)
20150721-2	145.3	69.2	62	7.06	38.5 (40)	1.16 x 10^4	0.224	–	–
20151119-4	152.6	68.9	59	6.90	32.1 (30)	1.06 x 10^4	0.179	4.51 (0.07)	–
20150722-1	174.9	69.6	55	6.83	13.8 (15)	9.06 x 10^3	0.995	–	–

965 **Table 1.** Continued

Run number [a]	Target			Impact velocity v_i, km s^{-1}	Impact angle θ[b], degree	Specific energy Q, J kg^{-1}	NLFM m_l/M_t[c]	Antipodal velocity V_a[d], m s^{-1}	α[e]
	Mass M_t, g	Diameter, mm	Porosity, %						
Head-on collision									
20161213-1	200.4	69.7	49	3.02	82.0 (80)	1.55 x 10^3	0.669	2.26 (0.004)	0.69 (0.03)
20161220-1	120.7	58.9	49	3.08	82.7 (80)	2.67 x 10^3	0.287	3.88 (0.04)	0.68 (0.01)
20161220-2	70.1	49.3	49	3.14	80.9 (80)	4.76 x 10^3	0.227	7.10 (0.16)	0.74 (0.02)
20170110-1	37.2	39.5	48	3.19	90.0 (90)	9.27 x 10^3	0.090	13.80 (0.22)	0.77 (0.04)
20150715-1	84.1	59.0	65	3.73	83.4 (80)	5.64 x 10^3	0.151	6.80 (0.02)	–
20150515-2*	50.3	49.2	63	3.74	88.7 (90)	9.43 x 10^3	0.109	9.98 (0.08)	0.86 (0.02)
20150715-2	27.4	40.3	64	3.83	81.6 (80)	1.81 x 10^4	0.054	16.27 (0.09)	–
20161011-1	202.0	70.3	50	4.04	85.3 (90)	2.75 x 10^3	0.181	3.58 (0.06)	0.71 (0.01)
20161025-1	120.4	58.9	49	4.03	88.6 (90)	4.58 x 10^3	0.258	5.99 (0.05)	0.65 (0.01)
20161018-1	71.0	49.0	48	4.07	82.5 (80)	7.93 x 10^3	0.134	8.99 (0.01)	0.83 (0.02)
20161018-2	38.0	40.0	48	3.96	84.3 (80)	1.40 x 10^4	0.069	14.17 (0.10)	0.72 (0.02)
20151020-2	200.3	69.1	47	4.34	85.9 (90)	3.20 x 10^3	0.150	3.82 (0.05)	0.65 (0.03)
20151020-1	118.9	58.7	49	4.36	84.4 (80)	5.42 x 10^3	0.170	6.57 (0.13)	0.86 (0.04)
20151013-1*	70.1	48.7	47	4.36	80.5 (80)	9.22 x 10^3	0.067	10.26 (0.01)	0.71 (0.02)
20151027-1	37.5	39.9	49	4.33	84.9 (90)	1.70 x 10^4	0.033	17.47 (0.18)	0.81 (0.21)
20141209-4	163.0	68.6	56	7.13	86.6 (90)	1.06 x 10^4	0.093	8.39 (0.06)	0.71 (0.01)
20150715-3	51.0	49.4	63	6.95	80.3 (80)	3.21 x 10^4	0.044	22.72 (0.06)	–
20150715-4	27.0	39.9	63	6.91	86.5 (90)	5.99 x 10^4	0.025	33.25 (1.19)	–

966

a: Asterisks (*) indicate the results shown in Fig. 5b. Plus signs (+) indicate the results shown in Fig. 10a.

b: The numbers without parentheses indicate the impact angle measured by using the images observed by a high-speed camera or a shutter camera. The numbers in parentheses indicate the impact angle used in the text.

c: NLFM means the normalized largest fragment mass, which is the largest fragment mass normalized by the original target mass.

d: The numbers in parentheses indicate the error.

e: α is the power law index on the power law equation showing the mass frequency distributions of impact fragments. The numbers in parentheses indicate the error.

974 **Table 2.** Experimental conditions and results for glass targets

Run number [a]	Target		Impact velocity v_i, km s^{-1}	Impact angle θ[b], degree	Specific energy Q, J kg^{-1}	NLFM m_l/M_t[c]	Antipodal jet velocity V_{jet}[c], m s^{-1}	α[e]
	Mass M_t, g	Diameter, mm						
Oblique impact: Target diameter = 80 mm, Impact velocity ~4.3 km s^{-1}								
20151119-1	671.3	79.6	4.19	76.6 (75)	8.88×10^2	0.631	159.90 (1.40)	0.89 (0.01)
20151028-1	662.8	79.3	4.34	59.1 (60)	9.64×10^2	0.679	197.04 (4.00)	0.92 (0.01)
20151008-2	626.8	77.9	4.38	46.8 (45)	1.04×10^3	0.833	163.52 (n.d.)	0.98 (0.01)
20151028-2	664.1	79.4	4.41	37.2 (40)	9.96×10^2	0.868	–	1.08 (0.01)
20151111-1	669.1	79.6	4.25	21.8 (20)	9.18×10^2	0.944	–	1.03 (0.02)
20151125-1	663.7	79.3	4.30	14.8 (15)	9.47×10^2	0.973	26.93 (n.d.)	0.99 (0.03)
Oblique impact: Target diameter = 50 mm, Impact velocity ~4.3 km s^{-1}								
20151029-2	163.1	50.1	4.32	72.9 (75)	3.88×10^3	0.046	210.64 (1.08)	1.03 (0.02)
20151008-1	163.7	50.2	4.39	57.3 (60)	3.99×10^3	0.028	153.76 (1.92)	1.00 (0.02)
20151022-1*	164.4	50.2	4.25	58.9 (60)	3.73×10^3	0.059	186.20 (3.58)	0.94 (0.02)
20151118-1*[+]	162.7	50.0	3.96	41.9 (40)	3.26×10^3	0.203	150.38 (4.61)	0.88 (0.03)
20151022-2	160.0	49.8	4.39	32.1 (30)	4.08×10^3	0.479	164.90 (n.d.)	0.92 (0.02)
20151119-2*[+]	154.8	49.3	4.37	28.4 (30)	4.19×10^3	0.562	156.64 (12.20)	0.95 (0.03)
20151202-1*[+]	164.6	50.2	4.28	14.8 (15)	3.78×10^3	0.780	–	0.81 (0.01)
Oblique impact: Target diameter = 80 mm, Impact velocity ~5.9 km s^{-1}								
20170208-1	658.6	79.0	5.93	57.4 (60)	1.81×10^3	0.216	188.32 (8.07)	0.87 (0.01)
20170208-2	637.5	78.2	5.86	47.0 (45)	1.83×10^3	0.517	220.30 (2.63)	0.90 (0.01)
Oblique impact: Target diameter = 30 mm, Impact velocity ~4.9 km s^{-1}								
20160107-1	32.3	29.2	4.87	76.6 (75)	2.49×10^4	0.005	196.34 (3.79)	–

975 **Table 2.** Continued

Run number [a]	Target		Impact velocity v_i, km s^{-1}	Impact angle θ[b], degree	Specific energy Q, J kg^{-1}	NLFM m_l/M_t[c]	Antipodal jet velocity V_{jet}[c], m s^{-1}	α[e]
	Mass M_t, g	Diameter, mm						
Head-on collision								
20151209-1	668.7	79.5	2.17	89.5 (90)	2.39 x 10^2	0.943	56.20 (1.27)	–
20151203-2	164.9	50.3	2.13	81.6 (80)	9.32 x 10^2	0.586	111.66 (1.20)	–
20151007-1	586.5	76.0	4.17	83.7 (80)	1.00 x 10^3	0.733	–	0.93 (0.01)
20151001-1*+	164.7	50.3	4.14	80.5 (80)	3.53 x 10^3	0.040	177.12 (0.73)	0.93 (0.02)
20160107-2	669.0	79.6	4.93	80.8 (80)	1.24 x 10^3	0.391	264.03 (3.17)	1.00 (0.01)
20160106-1	278.8	59.5	4.94	88.6 (90)	2.97 x 10^3	0.029	211.27 (3.97)	1.13 (0.04)
20151202-2	655.6	79.0	6.00	84.4 (80)	1.86 x 10^3	0.210	223.65 (n.d.)	–
20170207-1	658.9	79.0	5.88	84.5 (90)	1.78 x 10^3	0.189	201.39 (3.24)	0.87 (0.01)
20151203-1	163.7	50.2	5.95	86.8 (90)	7.34 x 10^3	0.015	255.71 (n.d.)	–

976

977 a: Asterisks(*) indicate the results shown in Figs. 5c and 5d. Plus signs (+) indicate the results shown in Fig. 10b.

978 b: The numbers without parentheses indicate the impact angle measured by using the images observed by a high-speed camera or a shutter camera.

979 The numbers in parentheses indicate the impact angle used in the text.

980 c: NLFM means the normalized largest fragment mass, which is the largest fragment mass normalized by the original target mass.

981 d: The numbers in parentheses indicate the error. “n.d.” means “not determined”.

982 e: α is the power law index on the power law equation showing the mass frequency distribution of impact fragments. The numbers in parentheses

983 indicate the error.

984 **Table 3.** Parameters p_1 and q_1 of Eq. (2) and impact strength Q^* at head-on

985 collisions (θ =90° and 80°)

986

Target	p_1	q_1	Q^* [J kg^{-1}]
Porous gypsum: this study	2.32 (0.31)	0.84 (0.08)	1.33 (0.47) × 10^3
Glass: this study	5.82 (0.70)	2.02 (0.21)	1.07 (0.19) × 10^3
Porous gypsum: *Okamoto and Arakawa* [2009]	2.66 (0.55)	0.87 (0.14)	2.42 (0.84) × 10^3
Basalt: *Fujiwara and Tsukamoto* [1980]	4.40 (0.68)	1.53 (0.18)	1.17 (0.78) × 10^3

987 Numbers in parentheses are the standard deviation.

988 The parameters p_1 and q_1 in this study were obtained at the m_l/M_t <0.75.

989 **Table 4.** Parameters p_2 and q_2 of Eq. (4) and effective impact strength ${Q_{\rm eff}}^*$

990

Target	Range of $m_{\rm l}/M_{\rm t}$ (NLFM)	p_2	q_2	${Q_{\rm eff}}^*$ [J kg^{-1}]
Porous gypsum: this study	< 0.75	2.02 (0.22)	0.76 (0.06)	1.14 (0.47) × 10^3
Glass: this study	> 0.75	0.12 (0.10)	0.08 (0.04)	9.07 (2.30) × 10^2
	< 0.75	4.66 (0.39)	1.68 (0.12)	
Basalt: *Fujiwara and Tsukamoto* [1980]	–	4.17 (0.40)	1.50 (0.11)	9.42 (4.08) × 10^2

991 Numbers in parentheses are the standard deviation.

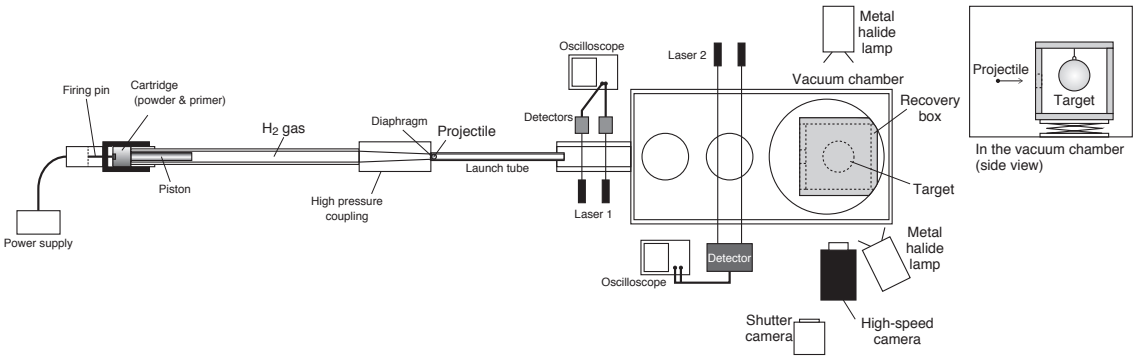

992

993 Fig. 1

994 Yasui et al.

995

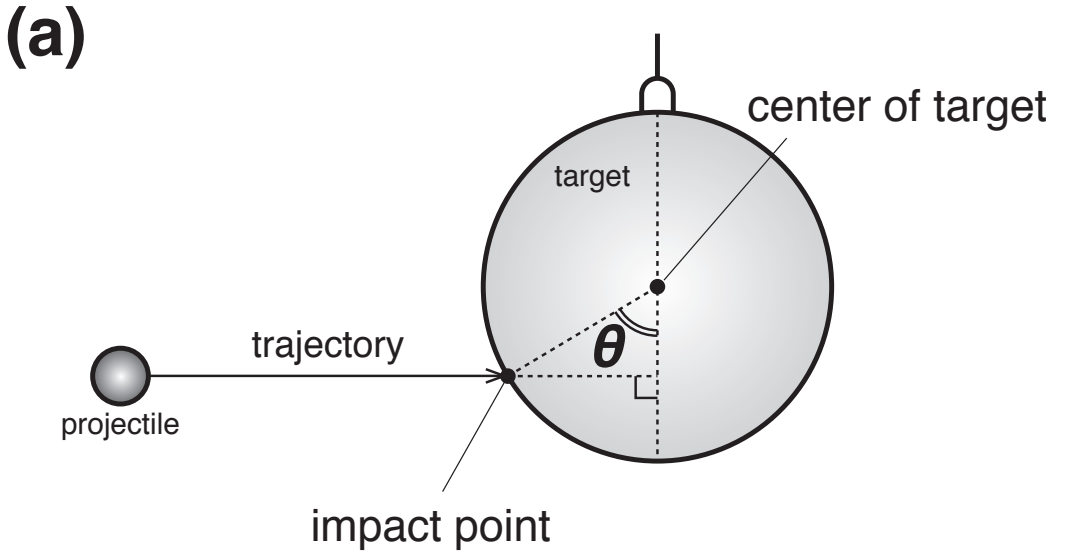

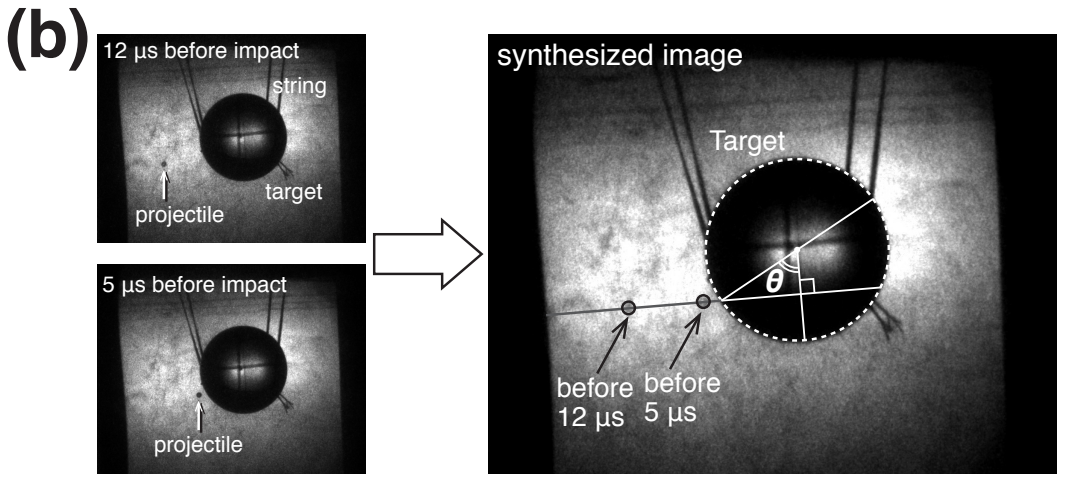

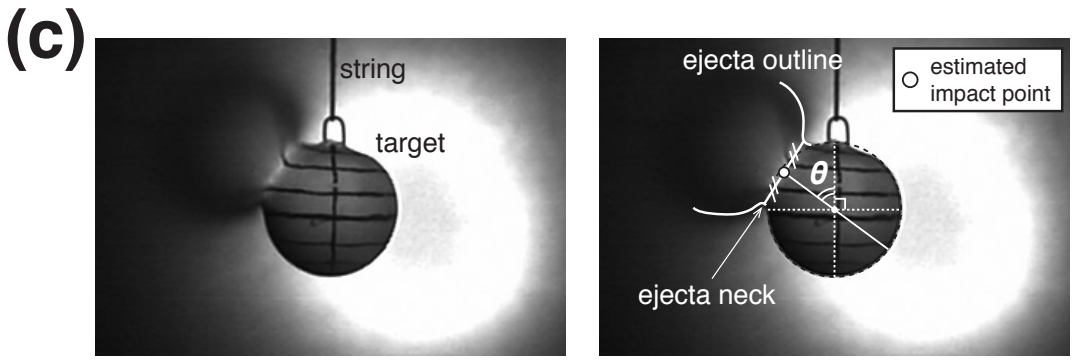

996

997 Fig. 2

998 Yasui et al.

999

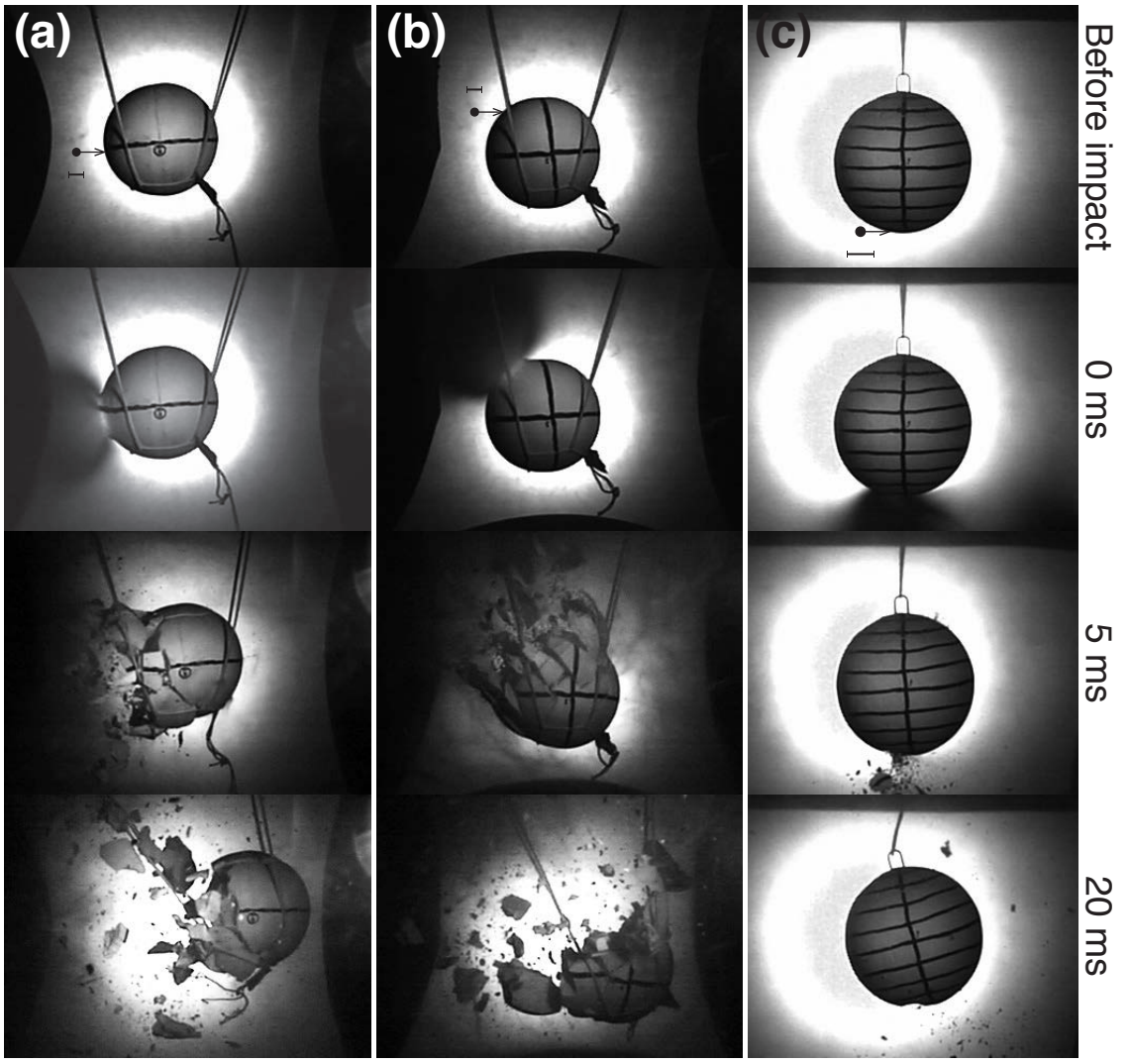

Fig. 3a–c

Yasui et al.

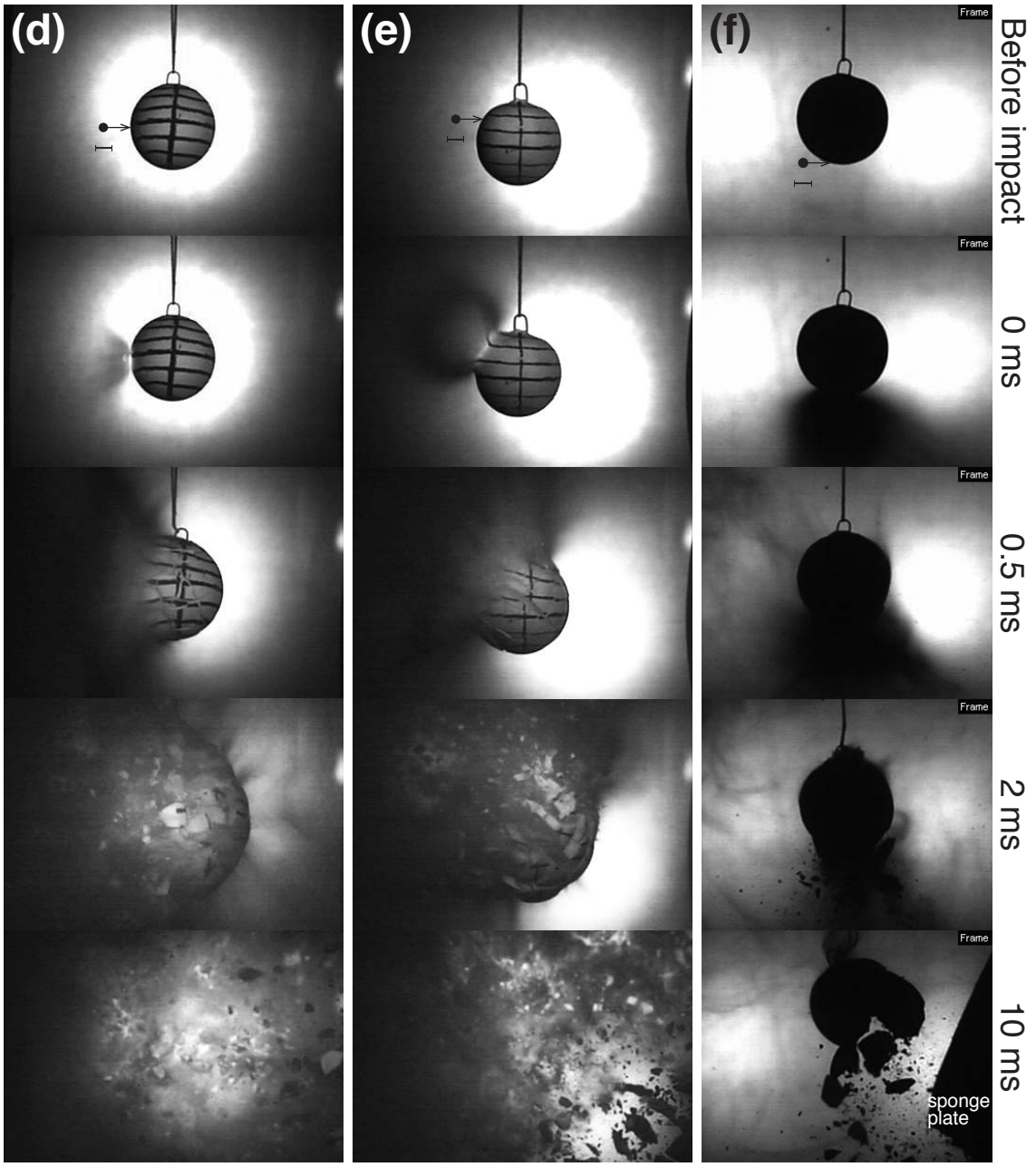

Fig. 3d–f

Yasui et al.

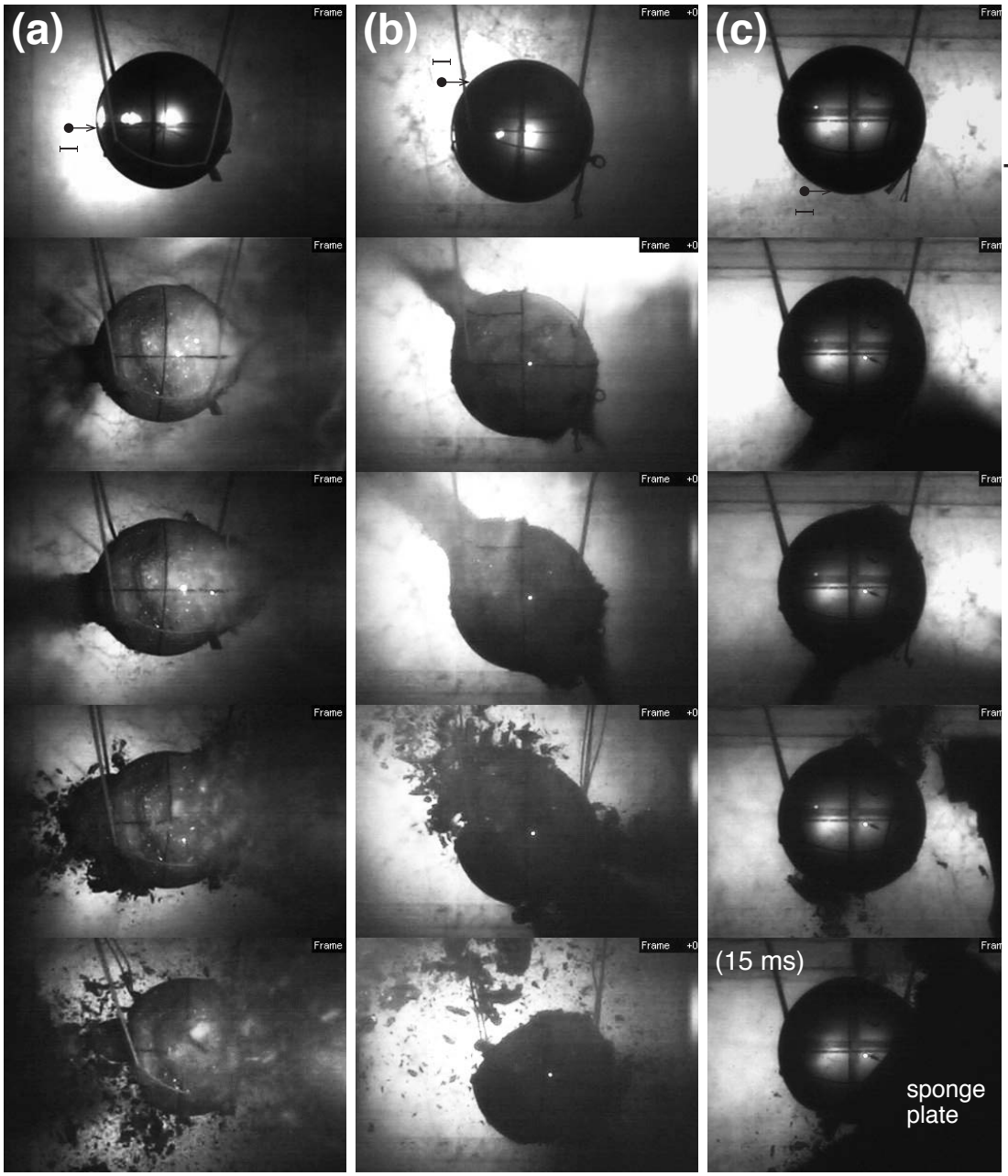

Fig. 4a–c

Yasui et al.

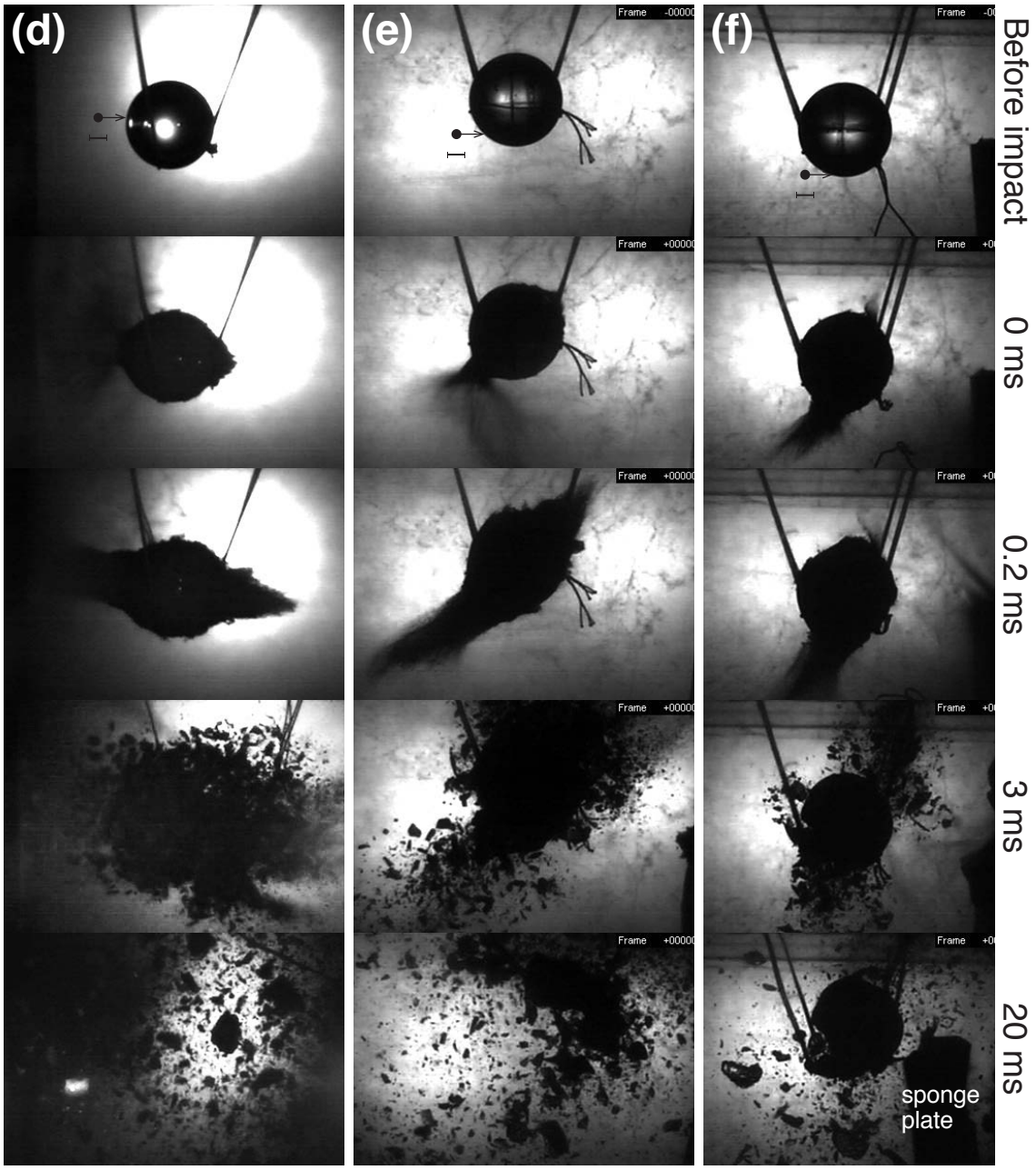

Fig. 4d–f

Yasui et al.

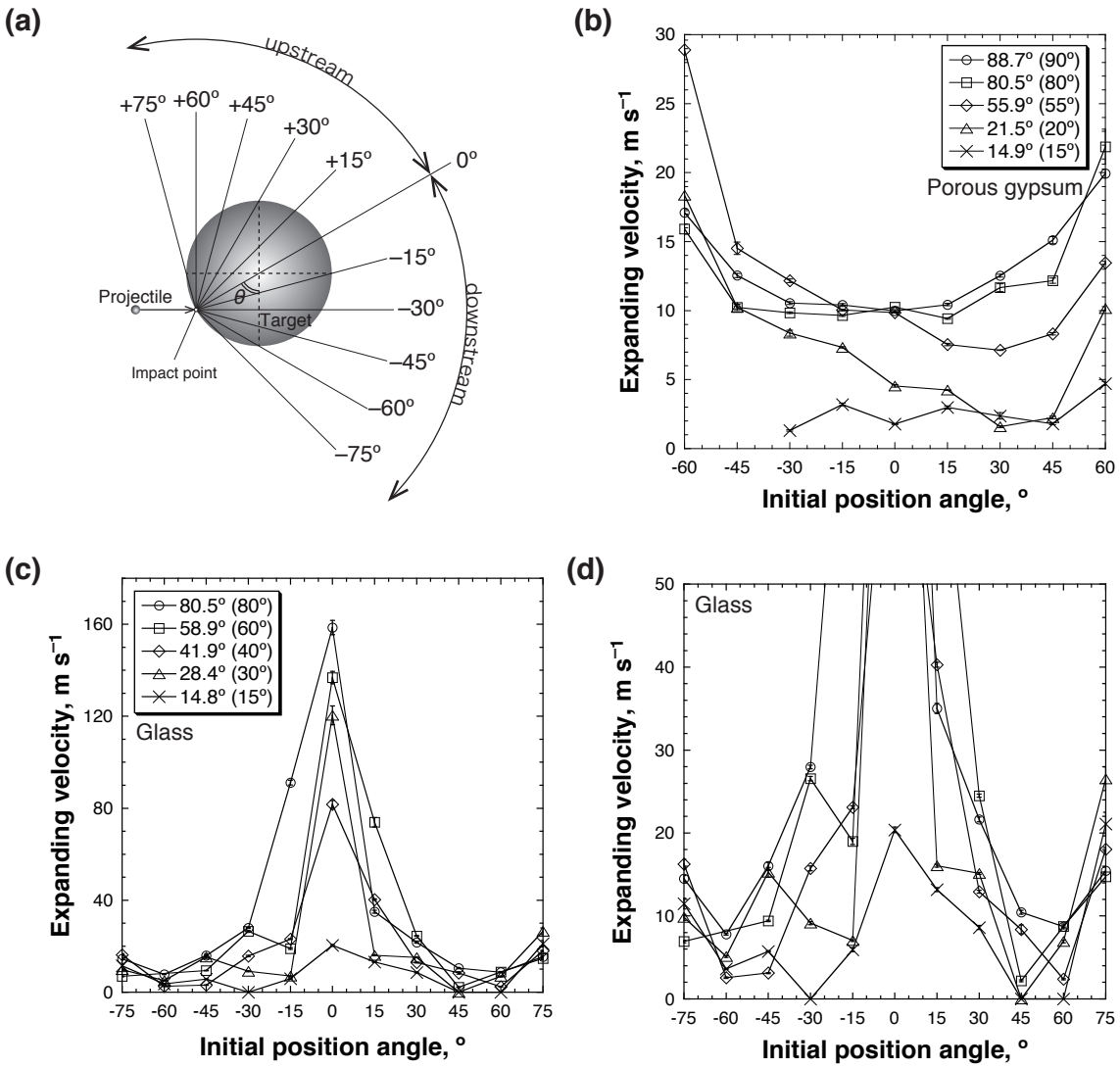

1015

1016 Fig. 5

1017 Yasui et al.

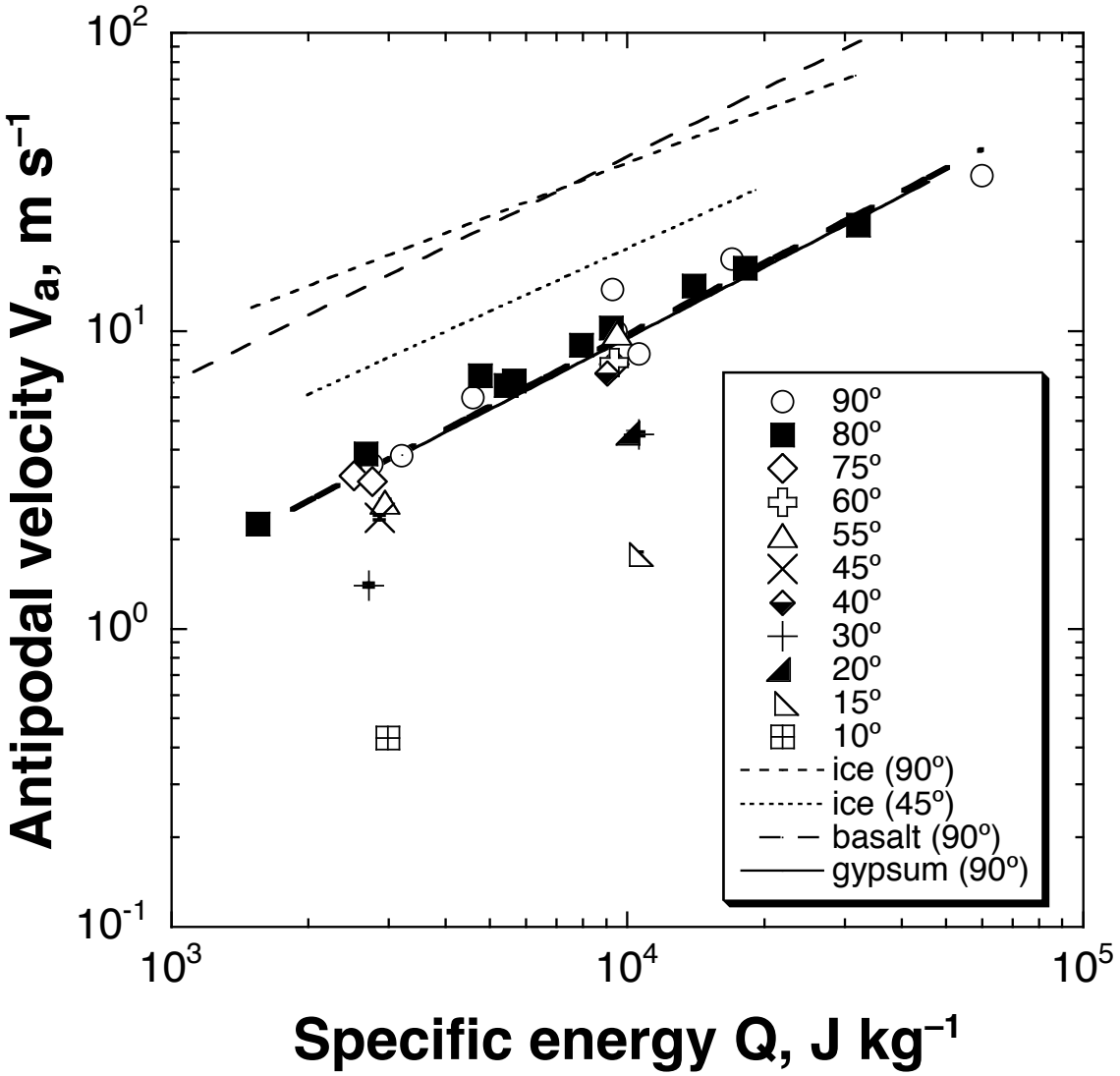

1018

1019 Fig. 6

1020 Yasui et al.

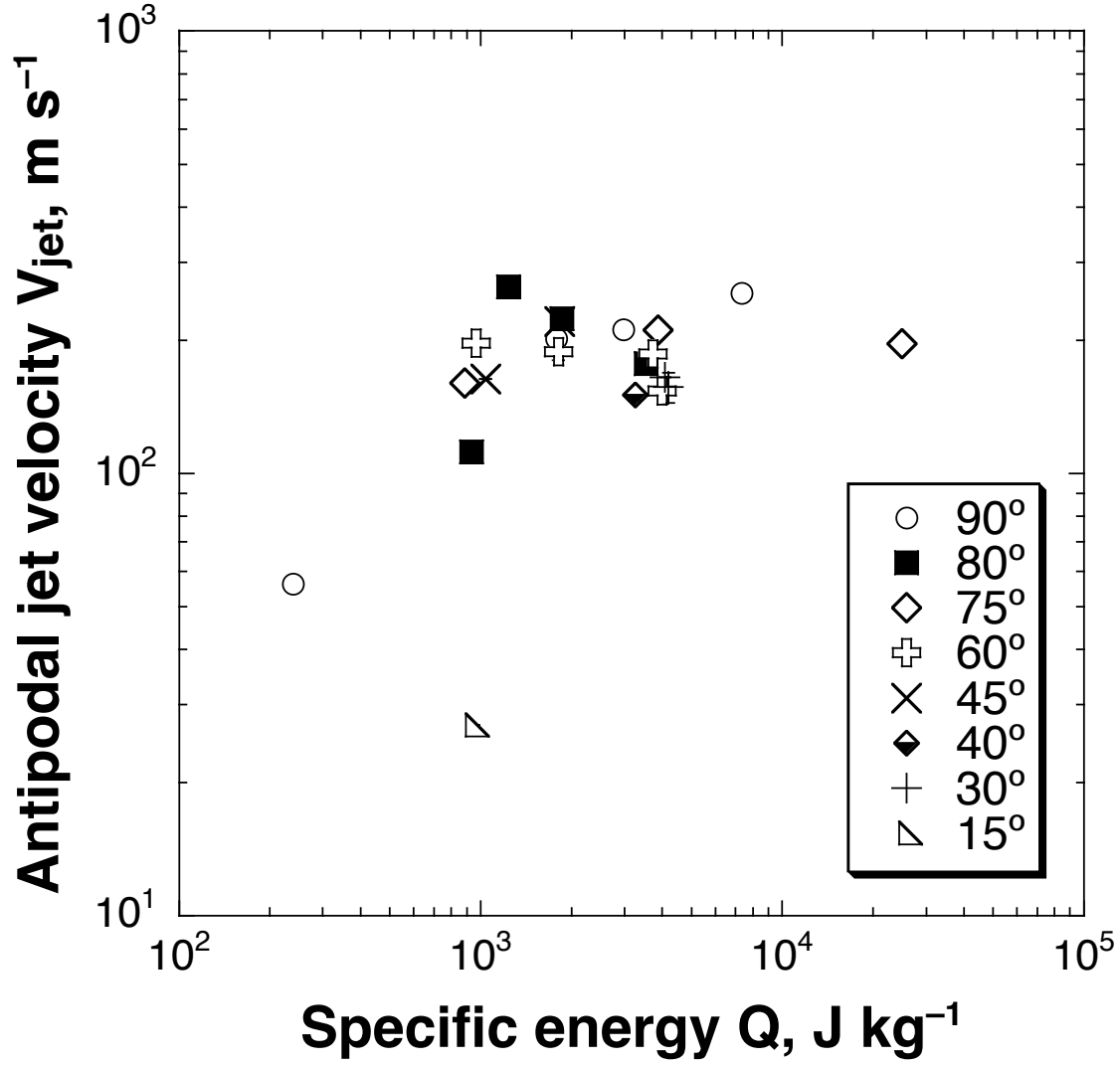

1021

1022 Fig. 7

1023 Yasui et al.

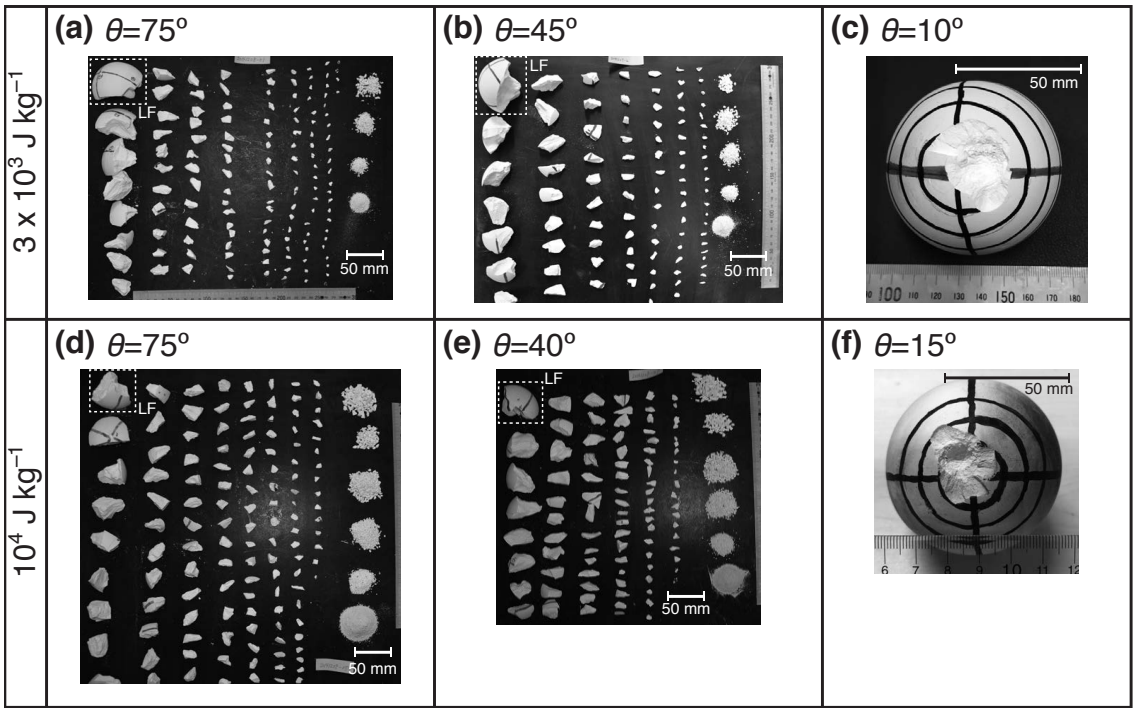

1024

1025 Fig. 8

1026 Yasui et al.

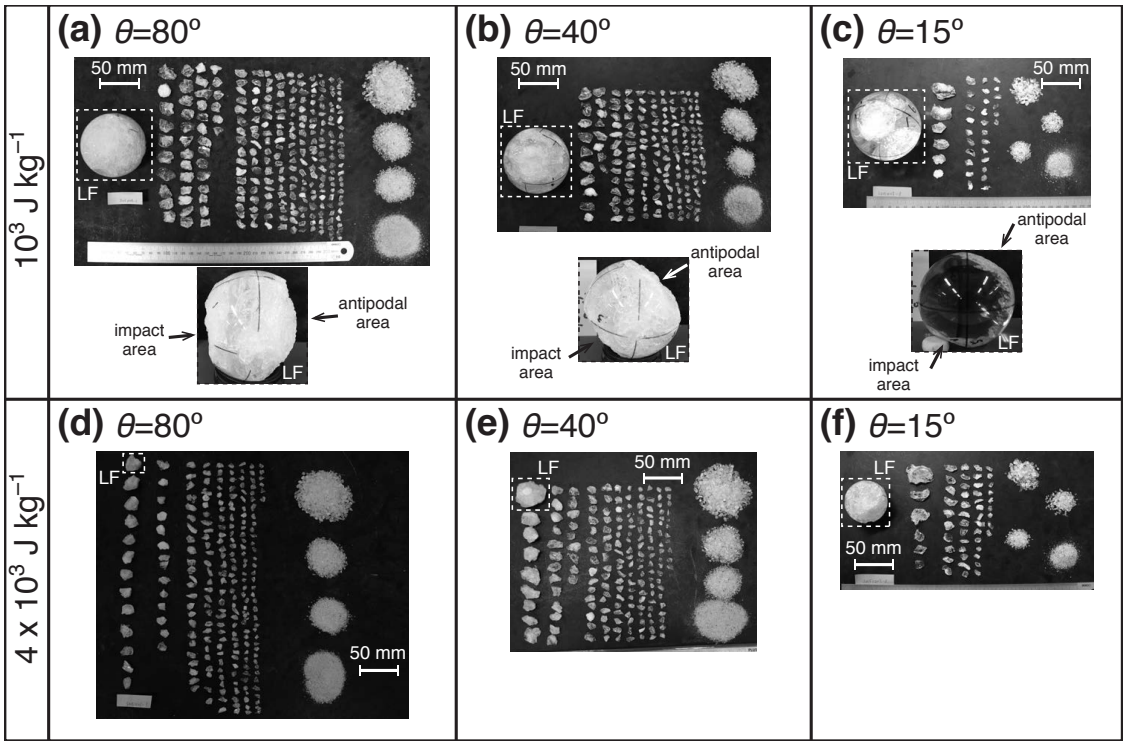

1027

1028 Fig. 9

1029 Yasui et al.

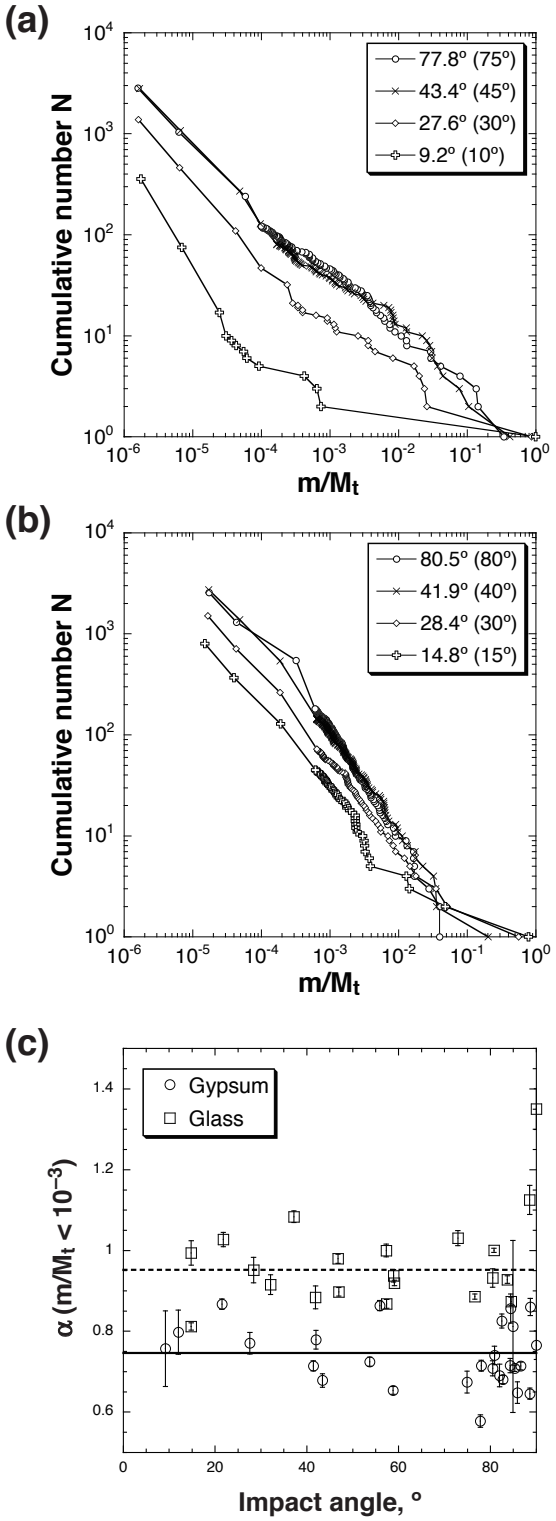

1030

1031 Fig. 10

1032 Yasui et al.

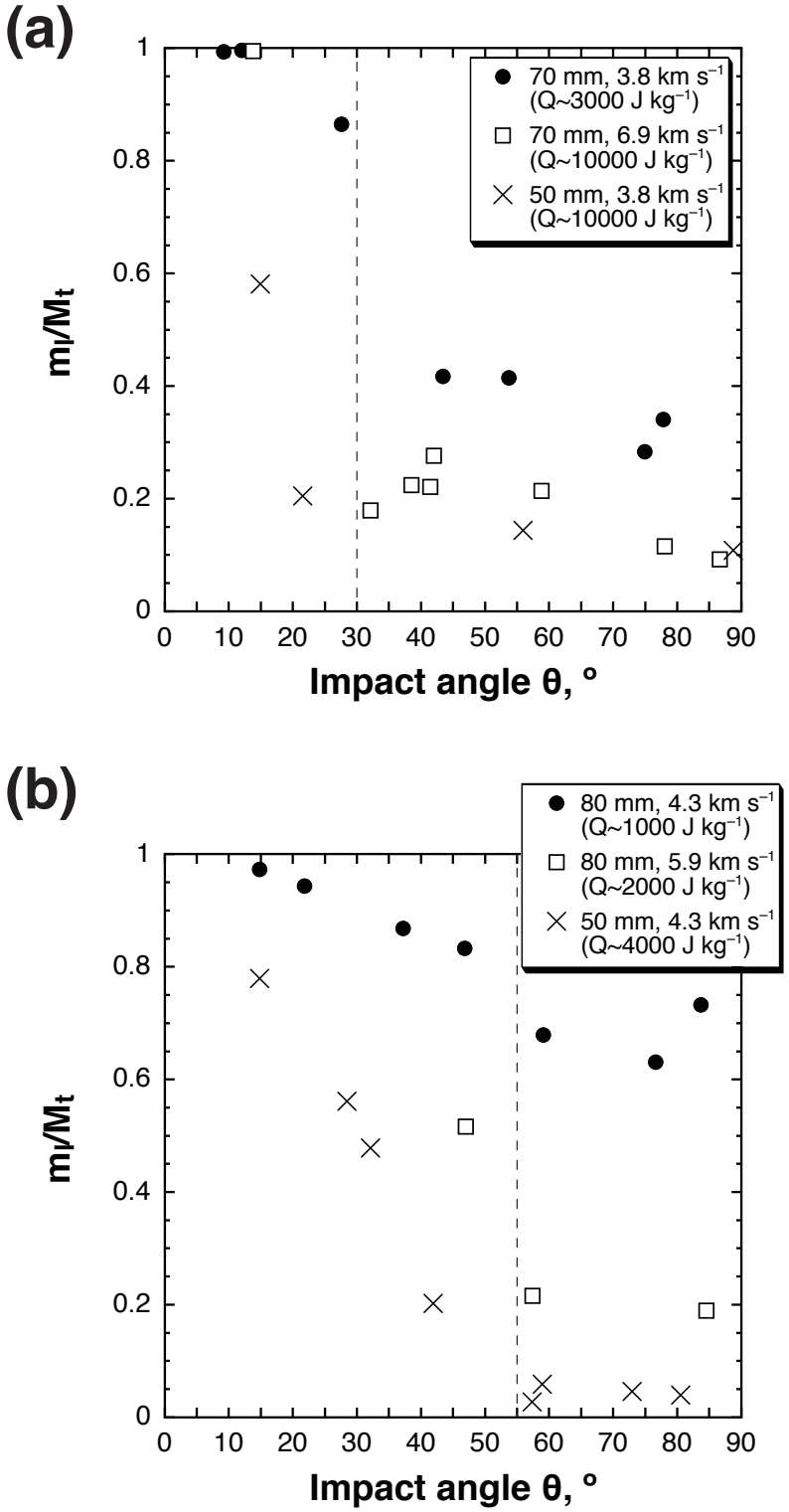

1033

1034 Fig. 11

1035 Yasui et al.

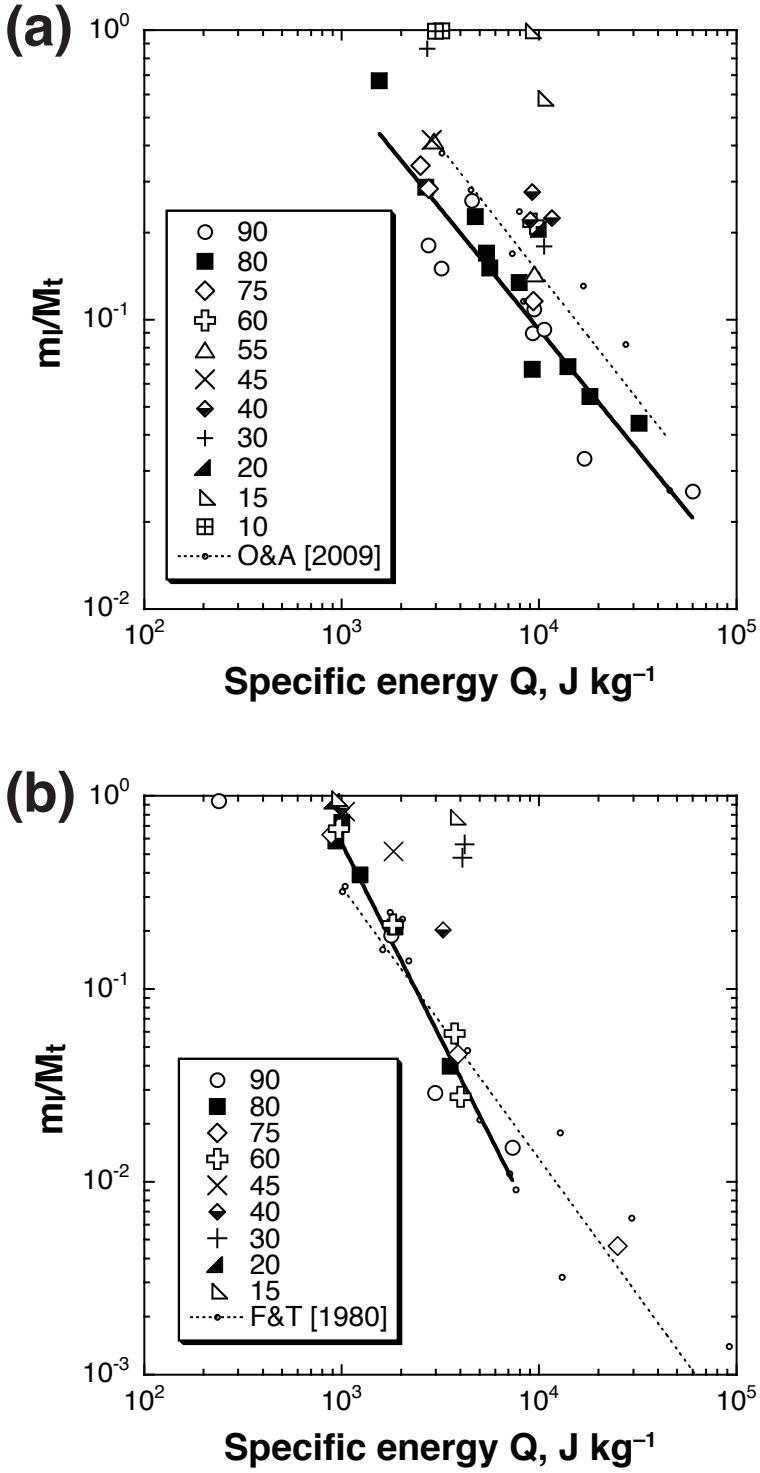

1036

1037 Fig. 12

1038 Yasui et al.

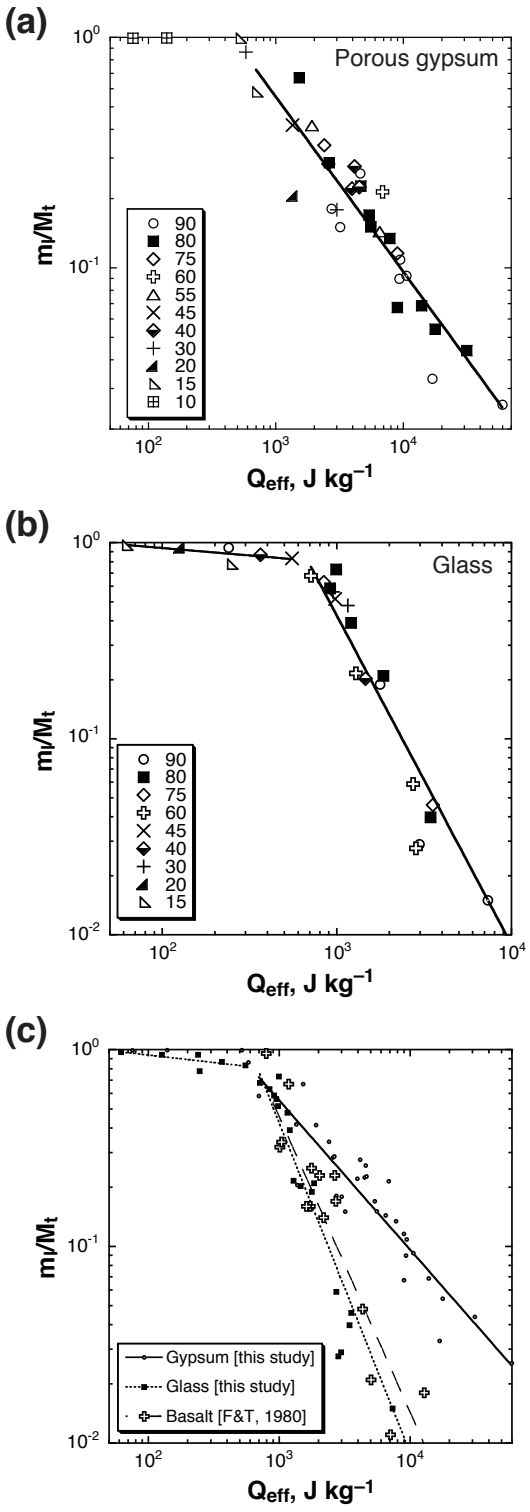

1039

1040 Fig. 13

1041 Yasui et al.

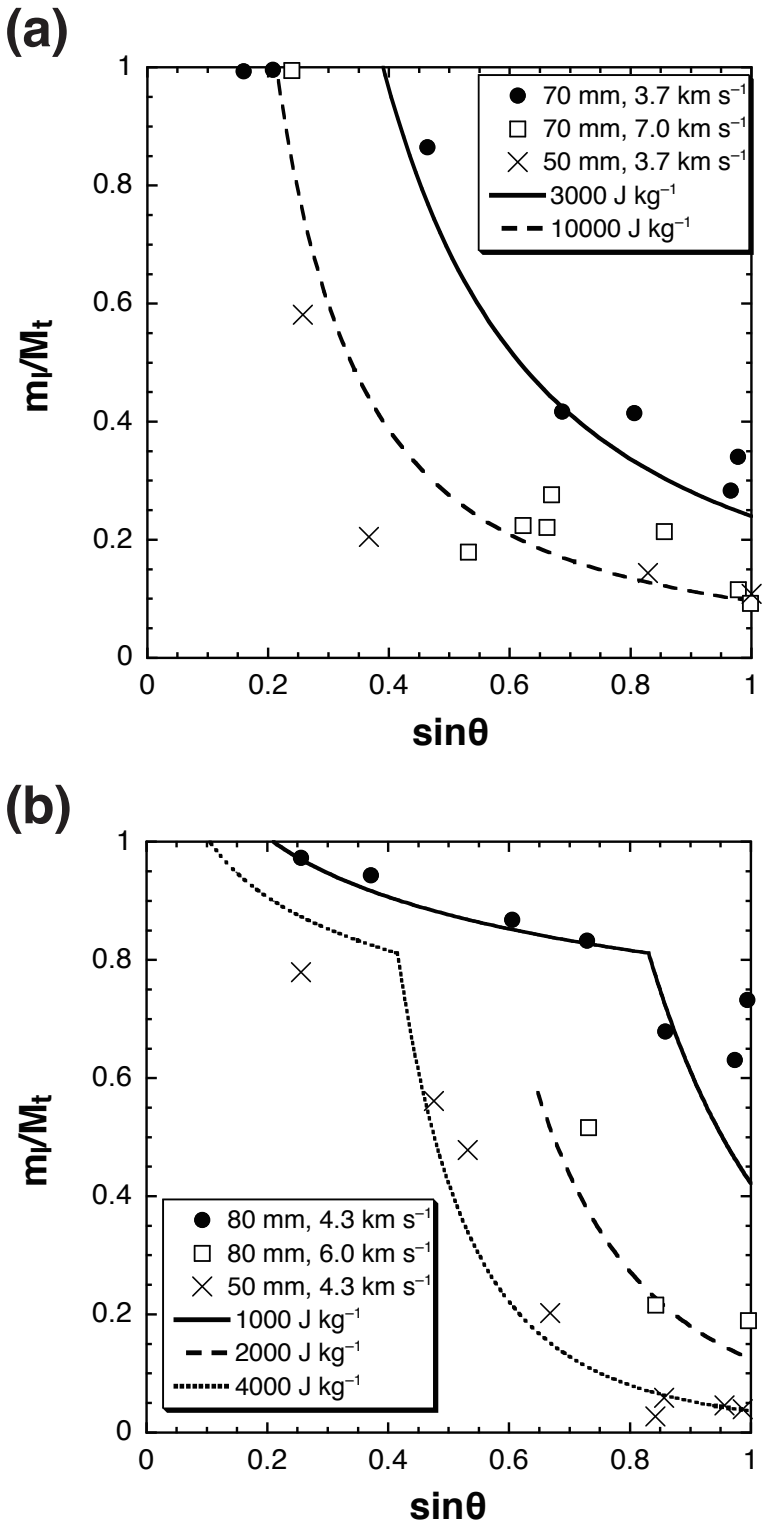

1042

1043 Fig. 14

1044 Yasui et al.

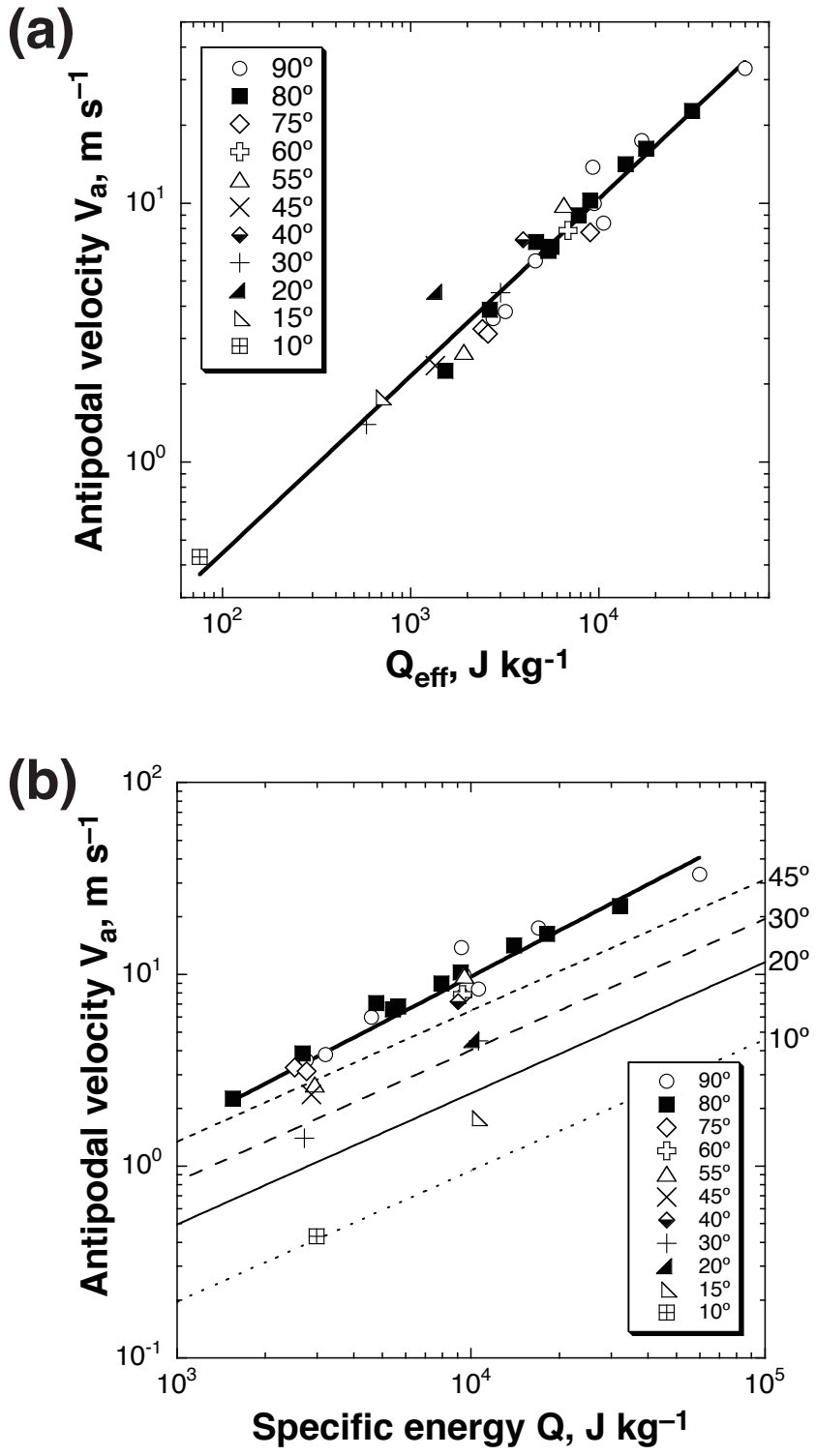

1045

1046 Fig. 15

1047 Yasui et al.

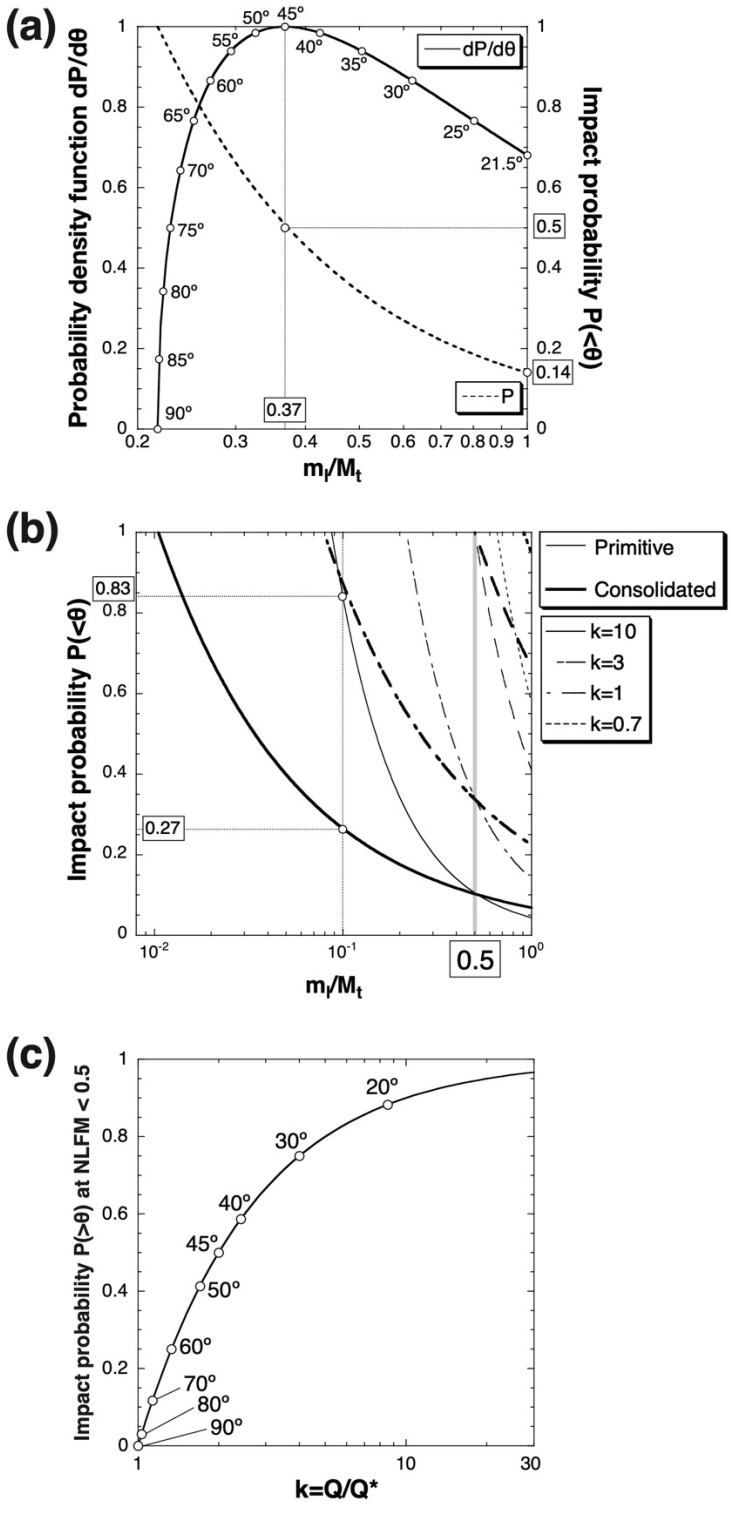

Fig. 16

Yasui et al.